Title
Grazing-Incidence Monochromators for Third Generation Synchrotron Radiation Sources

Journal
Vacuum Ultraviolet Spectroscopy, II

Author
Padmore, H.A.

Publication Date
1998

LBNL-40652
UC-410

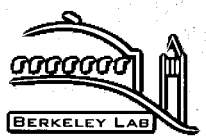

ERNEST ORLANDO LAWRENCE
BERKELEY NATIONAL LABORATORY

Grazing-Incidence Monochromators for Third Generation Synchrotron Radiation Sources

H.A. Padmore, M.R. Howells, and W.R. McKinney

Accelerator and Fusion Research Division

June 1997

Published as
a chapter in
Techniques of Vacuum Ultraviolet Physics
J.A. Samson and
D.A. Ederer, eds.,
Academic Press,
Orlando, FL, 1997

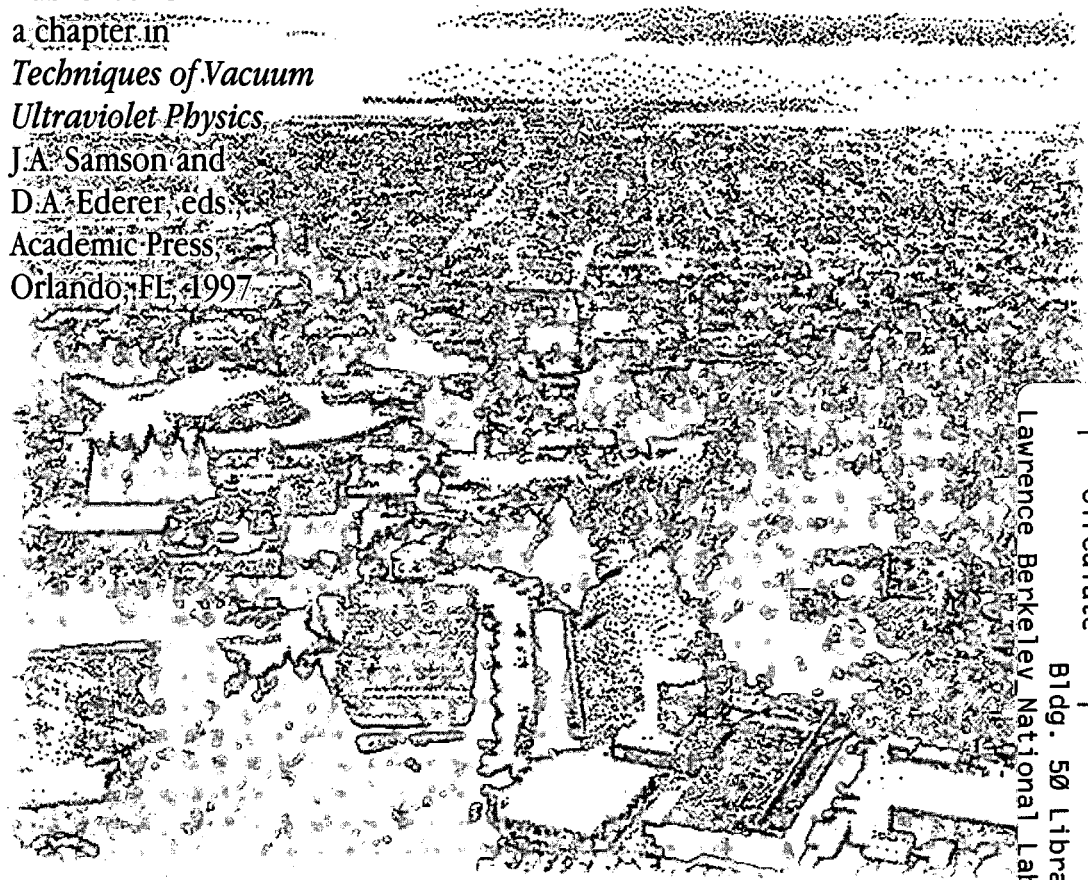

DISCLAIMER

LBNL-40652
LSBL-390
UC-410

Grazing-Incidence Monochromators for Third Generation Synchrotron Radiation Sources

H.A. Padmore, M.R. Howells, W.R. McKinney

Advanced Light Source
Lawrence Berkeley National Laboratory
University of California
Berkeley, California

*This work was supported by the Director, Office of Energy Research, Office of Basic Energy Sciences, Materials Sciences Division, of the U.S. Department of Energy, under Contract No. DE-AC03-76SF00098.

Grazing-Incidence Monochromators for Third Generation Synchrotron Radiation Sources

H. A. Padmore, M. R. Howells and W. R. McKinney

Advanced Light Source, 2-400, Lawrence Berkeley National Laboratory,
Berkeley, CA 94720, USA
(510) 486-5787

I. Introduction

In this article, we will discuss the foundations of modern vacuum ultraviolet (VUV) and soft x-ray (SXR) monochromator design based on the well-established theories of geometrical aberrations in grazing incidence optical systems and grating diffraction efficiency. We will restrict our treatment to topics of relevance to the construction of optical systems for third generation synchrotron radiation sources. These design considerations will be illustrated here by examples from the Advanced Light Source (ALS) and will show clearly how monochromator design is evolving, both for undulator and bending magnet sources and for several different applications in spectroscopy and microscopy.

It is clear from the many types of monochromator used today that a variety of solutions are possible within the prevailing optical design rules, and it is important to understand the historical development of these designs to predict where the future will take us and to see what the driving forces are. The evolution of the field is best seen through reviews and the many instrumentation conferences held over the years. In particular, the period of instrumentation for first generation machines can be seen in the reviews of Haensel and Kunz in 1967 [10] and by Madden in 1974 [24] in the conference proceedings of the International Symposium for Synchrotron Radiation Users edited by Marr and Munro in 1973 [25], and in the proceedings of the 4th International Conference on Vacuum Ultraviolet Radiation Physics in 1974 [20] The first international conference on synchrotron radiation instrumentation (SRI) in 1977, chaired by Wuilleumier and Farge [59], and the first US national conference on synchrotron radiation, chaired by Ederer and West in 1979 [7], heralded the era of the second-generation machines. The international conferences on SRI in Hamburg (1982) [51], Stanford (1985) [52], Tsukuba (1988) [53], and Chester (1991) [54] cover the period from operation of the second-generation machines, while the operation of the third-generation machines began roughly with the Stony Brook SRI meeting in 1994. During this period, all the monochromator designs used today emerged: the Petersen plane-

grating monochromator (PGM) [38-40] and its derivatives, the spherical-grating monochromator (SGM) [5, 6, 14, 31] and the variable-angle SGM [32, 36, 37] In a later section, these designs are discussed, particularly in relation to how considerations of focusing drive the efficiency of the optical system. The reviews by Gudat and Kunz [8], Johnson [19], Howells [15], West and Padmore [57], Peatman and Senf [37] and Padmore and Warwick [34] cover the operational periods of the first- to the third-generation machines.

The constraints on optical system designs go well beyond those traditionally imposed by strict considerations of resolving power. Although still important, the fact that modern spherical grating monochromators can routinely achieve a resolving power of 10^4 (one at the ALS has achieved $>6x10^4$), means that this aspect of the design is well understood and works as expected within limits set by optical manufacturing. However, other aspects are much less well-documented. We would highlight three main areas:

Optical matching: the high collimation of undulator radiation and the small source size of bending magnets on third-generation machines offer important opportunities in optical design for increasing light collection and efficiency. This is especially significant for beam lines where some form of microscopy is to be practiced at the endstation. Incorrect matching of the microscope optics to the source can lead to an enormous loss of flux.

Fexibility: the high cost of undulators and their associated high-power beamlines initially led to beamline designs in which the experimental needs of rather different communities—for example, high-resolution spectroscopists and high-spatial-resolution microscopists—were accommodated in a single instrument. This was by necessity a compromise, and it is now clear that beamlines with a single function can be designed with better performance and at less cost.

Applications: new applications of synchrotron radiation are changing the way that we must approach beamline design. In some experiments, access to an increased energy range is important. For example, in solid-state photoemission it is sometimes desirable to go to a low photon energy (<30 eV) to perform band mapping studies while being able to go to high photon energies (>1500 eV) to measure core-level shifts. In addition, it is often important to tune rapidly between the low- and high-energy regions, still preserving precise energy calibration. Although significant advances have been made in this area, several challenges remain. A new area of application is that of x-ray microscopy to problems in materials science. A particular thrust of work at the ALS is in systems directed toward the needs of the local microelectronics industry. These include microfocused x-ray photoelectron spectroscopy (micro-XPS) and x-ray absorption-based

photoelectron emission microscopy (X-PEEM). These have very different optical design parameters from spectroscopic beamlines. Moreover, the competitive environment of analytical instrumentation drives many design decisions based on "return on investment." The need is for systems that are dedicated full time to analytical measurements, functioning rather like a standard instrument operating with a laboratory radiation source. This means that the costs must be comparable to commercial instruments and that capacity can easily be increased by simple replication.

In the examples later, we describe an SGM undulator beamline and two "application-specific" bending magnet beamlines for micro-XPS and X-PEEM. We first describe aberration theory of grazing incidence mirrors and gratings and apply this in detail to the design of an ALS undulator beam line for ultra-high-resolution spectroscopy. We then present a guide for optimizing diffraction efficiency and discuss the special requirements of the various forms of x-ray microscopy and illustrate the foregoing principles with examples from the ALS.

II. Grating theory

The first type of focusing grating to be analyzed theoretically was that formed by the intersection of a substrate surface with a set of parallel equi-spaced planes: the so-called "Rowland grating." The full optical theory of such gratings was in place before 1967 and was reviewed in the first edition of this book. The theory of spherical-grating systems was established first [23, 45, 46], and was described comprehensively in the 1945 paper of Beutler [2]. Treatments of toroidal [9] and ellipsoidal [27] gratings came later, as reviewed in 1965 by Welford [55] and in 1985 by Hunter [17].

The major developments since 1967 have been in the use of nonuniformly spaced grooves. The application of holography to spectroscopic gratings was first reported by Rudolph and Schmahl [47, 48] and by Labeyrie and Flamand [21]. Its unique opportunities for optical design were developed initially by Jobin-Yvon [42] and by Namioka and coworkers [29, 30]. A different approach was followed by Harada [11] and others, who developed the capability to produce gratings with variable-line spacing through the use of a computer-controlled ruling engine. The application of this class of gratings to spectroscopy has been developed still more recently, principally by Hettrick [13].

In this section we will give a treatment of grating theory up to sixth order in the optical path, which is applicable to any substrate shape and any groove pattern that can be produced by holography or by ruling straight grooves with (possibly) variable spacing.

A. Calculation of the path function for a Rowland grating

Following normal practice, we will analyze the imaging properties of gratings by means of the path function F. The most comprehensive account of this method is given in the paper by Noda et al [30]. We begin, without knowing anything about where the rays will go, by making a purely geometrical calculation of the path length $\langle \mathrm{AP} \rangle + \langle \mathrm{PB} \rangle$ from any point A(x, y, z) to any point B(x', y', z') via a variable point P(ξ, w, l) on the grating surface. We suppose that the zeroth groove (of width d_0) passes through O (the grating pole) while the nth groove passes through P. The overall notation, which is roughly that of Noda et al. [30], is explained in Fig. 1. Since we are interested in a *diffracted* beam in mth order, we include the term $mn\lambda$ in the path function so that F changes by an additional m waves for each groove moved by P when the position of P is allowed to vary [1]. The sign conventions we use are similar to those used in the first edition of this book. That is,, λ, d_0, and α are positive, and α and β are of opposite sign if they are on opposite sides of the normal. Inside order is considered positive and the directions of the ingoing ray and of increasing n are both toward $+y$.

We consider first the case of a Rowland grating since it will be simple to extend the treatment of this case to cover the other interesting ones. For a Rowland grating, F is given by

$$F = \langle \mathrm{AP} \rangle + \langle \mathrm{PB} \rangle + mn\lambda = \langle \mathrm{AP} \rangle + \langle \mathrm{PB} \rangle + \frac{m\lambda}{d_0} w \tag{1}$$

where

$$\langle \mathrm{AP} \rangle = \sqrt{(x-\xi)^2 + (y-w)^2 + (z-l)^2} \tag{2}$$

and $\langle \mathrm{PB} \rangle$ equals a similar expression with x', y', and z'. We now substitute for x, y, and ξ (see Fig. 1) in Eq. (2) according to

$$x = r\cos\alpha, \quad y = r\sin\alpha, \quad \xi = \sum_{ij} a_{ij} w^i l^j, \tag{3}$$

where r and α are constants and the summation replacing ξ expresses the shape of the grating surface. We then expand $\langle \mathrm{AP} \rangle$ as a Maclaurin series in w, l, and z,

$$\langle \mathrm{AP} \rangle = \sum_{n=0}^{\infty} \frac{1}{n!} \left\{ w\frac{\partial}{\partial w} + l\frac{\partial}{\partial l} + z\frac{\partial}{\partial z} \right\}^n \langle \mathrm{AP} \rangle \Big|_{0,0,0} \equiv \sum_{ijk} C_{ijk} w^i l^j z^k, \tag{4}$$

and use algebraic software (Mathematica™) [58] to compute the coefficients C_{ijk}, which are functions of α, r, and the a_{ij}'s. Applying the same method to $\langle \mathrm{PB} \rangle$ as well, Eq. (1) now becomes

$$F = \sum_{ijk} C_{ijk}(\alpha, r) w^i l^j z^k + \sum_{ijk} C_{ijk}(\beta, r') w^i l^j z'^k + \frac{m\lambda}{d_0} w, \tag{5}$$

which can be written

$$\begin{aligned} F &= \sum_{ijk} F_{ijk} w^i l^j \\ \text{where } F_{ijk} &= z^k C_{ijk}(\alpha, r) + z'^k C_{ijk}(\beta, r') \\ \text{except } F_{100} &= C_{100}(\alpha, r) + C_{100}(\beta, r') + \frac{m\lambda}{d_0}. \end{aligned} \tag{6}$$

The coefficient F_{ijk} is related to the strength of the i,j aberration of the wavefront diffracted by the grating. The coefficients C_{ijk} are given up to sixth order in Table I where the following notation is used:

$$\begin{aligned} T &= T(r,\alpha) = \frac{\cos^2\alpha}{r} - 2a_{20}\cos\alpha \quad S = S(r,\alpha) = \frac{1}{r} - 2a_{02}\cos\alpha \\ T' &= T(r',\beta) \qquad\qquad S' = S(r',\beta) \end{aligned} \tag{7}$$

To use the C_{ijk}'s, one must also have the a_{ij}'s and these are given to sixth order for ellipses and toroids [43] in Tables II and III, respectively. The a_{ij}'s for spheres, circular cylinders, paraboloids and hyperboloids can also be obtained from Tables II and III by suitable choices of the parameters r, r' and θ.

Table I: Coefficients C_{ijk} of the expansion of F [Eq. (4) et seq.][a]

$$C_{011} = -\frac{1}{r} \qquad C_{020} = \frac{S}{2}$$

$$C_{022} = -\frac{S}{4r^2} - \frac{1}{2r^3} \qquad C_{031} = \frac{S}{2r^2}$$

$$C_{040} = \frac{4a_{02}^2 - S^2}{8r} - a_{04}\cos\alpha \qquad C_{042} = \frac{a_{04}\cos\alpha}{2r^2} + \frac{3S^2 - 4a_{02}^2}{16r^3} + \frac{3S}{4r^4}$$

$$C_{100} = -\sin\alpha \qquad C_{102} = \frac{\sin\alpha}{2r^2}$$

$$C_{111} = -\frac{\sin\alpha}{r^2} \qquad C_{120} = \frac{S\sin\alpha}{2r} - a_{12}\cos\alpha$$

$$C_{131} = -\frac{a_{12}\cos\alpha}{r^2} + \frac{3S\sin\alpha}{2r^3} \qquad C_{122} = \frac{a_{12}\cos\alpha}{2r^2} - \frac{3S\sin\alpha}{4r^3} - \frac{3\sin\alpha}{2r^4}$$

$$C_{200} = \frac{T}{2} \qquad C_{140} = -a_{14}\cos\alpha + \frac{1}{2r}\left(2a_{02}a_{12} + a_{12}S\cos\alpha - a_{04}\sin 2\alpha\right) + \frac{\sin\alpha}{8r^2}\left(4a_{02}^2 - 3S^2\right)$$

$$C_{202} = -\frac{T}{4r^2} + \frac{\sin^2\alpha}{2r^3} \qquad C_{211} = \frac{T}{2r^2} - \frac{\sin^2\alpha}{r^3}$$

$$C_{031} = -\frac{1}{2r^3} \qquad C_{300} = -a_{30}\cos\alpha + \frac{T\sin\alpha}{2r}$$

$$C_{220} = -a_{22}\cos\alpha + \frac{1}{4r}\left(4a_{20}a_{02} - TS - 2a_{12}\sin 2\alpha\right) + \frac{S\sin^2\alpha}{2r^2}$$

$$C_{222} = \frac{1}{2r^2}a_{22}\cos\alpha + \frac{1}{8r^3}\left(3ST - 4a_{02}a_{20} + 6a_{12}\sin 2\alpha\right) + \frac{3}{4r^4}\left(T - 2S\sin^2\alpha\right) - \frac{3\sin^2\alpha}{r^5}$$

$$C_{231} = -\frac{1}{r^2}a_{22}\cos\alpha + \frac{1}{4r^3}\left(-3ST + 4a_{02}a_{20} - 6a_{12}\sin 2\alpha\right) + \frac{3S\sin^2\alpha}{r^4}$$

$$C_{240} = -a_{24}\cos\alpha + \frac{1}{2r}\left(a_{12}^2\sin^2\alpha + 2a_{04}a_{20} + a_{22}S\cos\alpha + a_{04}T\cos\alpha - a_{14}\sin 2\alpha + 2a_{02}a_{22}\right)$$
$$+ \frac{1}{16r^2}\left(-4a_{02}^2T - 8a_{02}a_{20}S + 12a_{12}S\sin 2\alpha + 3TS^2 + 16a_{02}a_{12}\sin\alpha - 8a_{04}\sin 2\alpha\right) + \frac{\sin^2\alpha}{4r^3}\left(2a_{02}^2 - 3S^2\right)$$

Table I (continued)

$$C_{302} = \frac{a_{30}\cos\alpha}{2r^2} - \frac{3T\sin\alpha}{4r^3} + \frac{\sin^3\alpha}{2r^4}$$

$$C_{311} = -\frac{a_{30}\cos\alpha}{r^2} + \frac{3T\sin\alpha}{2r^3} - \frac{\sin^3\alpha}{r^4}$$

$$C_{320} = -a_{32}\cos\alpha + \frac{1}{2r}\left(2a_{20}a_{12} + 2a_{30}a_{02} + a_{30}S\cos\alpha + a_{12}T\cos\alpha - a_{22}\sin 2\alpha\right)$$
$$+ \frac{1}{4r^2}\left(4a_{20}a_{02}\sin\alpha - 3ST\sin\alpha - 4a_{12}\cos\alpha\sin^2\alpha\right) + \frac{S\sin^3\alpha}{2r^3}$$

$$C_{400} = -a_{40}\cos\alpha + \frac{1}{8r}\left(4a_{20}^2 - T^2 - 4a_{30}\sin 2\alpha\right) + \frac{T\sin^2\alpha}{2r^2}$$

$$C_{402} = -\frac{1}{16r^3}\left(4a_{20}^2 + 3T^2 + 12a_{30}\sin 2\alpha\right) + \frac{a_{40}\cos\alpha}{2r^2} - \frac{3T\sin^2\alpha}{r^4} + \frac{\sin^4\alpha}{2r^5}$$

$$C_{411} = -\frac{a_{40}\cos\alpha}{r^2} + \frac{1}{8r^3}\left(4a_{20}^2 - 3T^2 - 12a_{30}\sin 2\alpha\right) + \frac{3T\sin^2\alpha}{r^4} - \frac{\sin^4\alpha}{r^5}$$

$$C_{420} = -a_{42}\cos\alpha + \frac{1}{2r}\left(2a_{20}a_{22} + 2a_{12}a_{30}\sin^2\alpha + 2a_{02}a_{40} - a_{32}\sin 2\alpha + a_{40}S\cos\alpha + a_{22}T\cos\alpha\right)$$
$$+ \frac{1}{16r^2}\left(-4a_{20}^2S - 8a_{02}a_{20}T + 3ST^2 + 12\sin 2\alpha\left(a_{30}S + a_{12}T\right) + 8\sin\alpha\left(2a_{02}a_{30} - 2a_{22}\sin 2\alpha + 2a_{12}a_{20}\right)\right)$$
$$+ \frac{1}{2r^3}\left(2a_{02}a_{20}\sin^2\alpha - 3ST\sin^2\alpha - 2a_{12}\cos\alpha\sin^3\alpha\right) + \frac{S\sin^4\alpha}{2r^4}$$

$$C_{500} = -a_{50}\cos\alpha + \frac{1}{2r}\left(2a_{20}a_{30} + a_{30}T\cos\alpha - a_{40}\sin 2\alpha\right) + \frac{\sin\alpha}{2r^2}\left(a_{20}^2 - a_{30}\sin 2\alpha\right) - \frac{3T^2\sin\alpha}{8r^2} + \frac{T\sin^3\alpha}{2r^3}$$

$$C_{600} = -a_{60}\cos\alpha + \frac{1}{2r}\left(a_{30}^2\sin^2\alpha + 2a_{20}a_{40} + a_{40}T\cos\alpha - a_{50}\sin 2\alpha\right)$$
$$+ \frac{1}{16r^2}\left(-4a_{20}^2T + T^3 + 16a_{20}a_{30}\sin\alpha + 12a_{30}T\sin 2\alpha - 16a_{40}\cos\alpha\sin^2\alpha\right)$$
$$+ \frac{1}{4r^3}\left(2a_{20}^2\sin^2\alpha - 3T^2\sin^2\alpha - 4a_{30}\cos\alpha\sin^3\alpha\right) + \frac{T\sin^4\alpha}{2r^4}$$

[a]The coefficients for which $i \le 6, j \le 4,\ k \le 2,\ i + j + k \le 6,\ j + k =$ even are included in this table. The only addition to those is C_{013}, which has some interest, because, when the system is specialized to be symmetrical about the x axis, it represents a Seidel aberration, namely distortion.

Table II: Ellipse coefficients Q_{ij} from which the a_{ij}'s of Eq. (3) are obtained[a] [43]

i \ j	0	1	2	3	4	5	6
0	0	0	1	0	$C/4$	0	$-C^2/8$
1	0	0	A	0	$3AC/4$	0	*
2	1	0	$\left(2A^2+C\right)/2$	0	$3C\left(4A^2+C\right)/8$	0	*
3	A	0	$A\left(2A^2+3C\right)/2$	0	*	0	*
4	$\left(4A^2+C\right)/4$	0	$\left(8A^4+24A^2C+3C^2\right)/8$	0	*	0	*
5	$A\left(4A^2+3C\right)/4$	0	*	0	*	0	*
6	$\left(8A^4+12A^2C+C^2\right)/8$	0	*	0	*	0	*

[a]If r, r' and θ are the object distance, image distance, and incidence angle to the normal, respectively, and

$$a_{20}=\frac{\cos\theta}{4}\left(\frac{1}{r}+\frac{1}{r'}\right),\quad A=\frac{\sin\theta}{2}\left(\frac{1}{r}-\frac{1}{r'}\right),\quad C=A^2+\frac{1}{rr'},$$

then

$$a_{ij}=a_{20}\frac{Q_{ij}}{\cos^j\theta}.$$

Table III: Toroid[a] a_{ij}'s of Eq. (3) [43]

j / i	**0**	**1**	**2**	**3**	**4**	**5**	**6**
0	0	0	$1/(2\rho)$	0	$1/(8R^3)$	0	$1/(16\rho^5)$
1	0	0	0	0	0	0	*
2	$1/(2R)$	0	$1/(4\rho R^2)$	0	$(2\rho+R)/(16\rho^3R^3)$	0	*
3	0	0	0	0	*	0	*
4	$1/(8R^3)$	0	$3/(16\rho R^4)$	0	*	0	*
5	0	0	*	0	*	0	*
6	$1/(16R^5)$	0	*	0	*	0	*

[a]R and ρ are the major and minor radii of the toroid.

Table IV: Coefficients n_{ijk} for a grating with variable line spacing [Eq. (12)]

$$n_{100} = 1/d_0$$

$$n_{200} = -\nu_1/2d_0$$

$$n_{300} = \left(\nu_1^2 - \nu_2\right)/3d_0$$

$$n_{400} = \left(-\nu_1^3 + 2\nu_1\nu_2 - \nu_3\right)/4d_0$$

$$n_{500} = \left(\nu_1^4 - 3\nu_1^2\nu_2 + \nu_2^2 + 2\nu_1\nu_3 - \nu_4\right)/5d_0$$

$$n_{600} = \left(-\nu_1^5 + 4\nu_1^3\nu_2 - 3\nu_1\nu_2^2 - 3\nu_1^2\nu_3 + 2\nu_2\nu_3 + 2\nu_1\nu_4 - \nu_5\right)/6d_0$$

B. Calculation of the path function for non-Rowland gratings

Next we calculate F for a grating with the groove pattern formed by holography using two coherent point sources, $C(r_C,\gamma,z_C)$ and $D(r_D,\delta,z_D)$. If the sources C and D are both real or both virtual, their equi-phase surfaces are a family of confocal hyperboloids of revolution about $\overline{CD}$. If one is real and the other virtual, then the equi-phase surfaces are the corresponding family of ellipsoids. This follows from the fact that interference fringes always bisect the angle between the *forward directions* of the rays forming them. Given that the recording process, at wavelength λ_0, delivers n fringes between O and P, we can write

$$n\lambda_0 = \left(\langle CP\rangle \pm \langle PD\rangle\right) - \left(\langle CO\rangle \pm \langle OD\rangle\right) \tag{8}$$

where the upper sign is for the ellipsoid case and the lower one for the hyperboloid. We can calculate $\langle CP\rangle$ and $\langle PD\rangle$ in the same way as $\langle AP\rangle$ and express them in the same way. Therefore, inserting n from Eq. (8) into Eq. (1) and dropping the second bracket of Eq. (8), which is just a constant, we obtain

$$F_{ijk} = z^k C_{ijk}(\alpha,r) + z'^k C_{ijk}(\beta,r') + \frac{m\lambda}{\lambda_0}\left\{z_C^k C_{ijk}(\gamma,r_C) \pm z_D^k C_{ijk}(\delta,r_D)\right\}. \tag{9}$$

Finally, we calculate F for a ruled grating with straight, parallel grooves that may have a variable spacing [26].

$$d(w) = d_0\left(1 + v_1 w + v_2 w^2 + \ldots\right). \tag{10}$$

In this case the calculation proceeds as for a Rowland grating up to Eq. (5), but now that n and d are functions of w (although not of l and z), the term $n(w)m\lambda$ must be expanded as a power series and will contribute, in principle, to all the F_{ijk}'s for which j=k=0. Therefore, recognizing that the local groove frequency is $1/d(w) = \partial n/\partial w$ and that $n(0)$=0, we have

$$n(w) = \sum_{i=1}^{\infty} n_{i00} w^i = \sum_{i=1}^{\infty} \frac{1}{i!}\frac{\partial^i n}{\partial w^i}\bigg|_0 w^i = \sum_{i=1}^{\infty} \frac{1}{i!}\frac{\partial^{i-1}}{\partial w^{i-1}}\left(\frac{1}{d_0\left(1 + v_1 w + v_2 w^2 + \ldots\right)}\right)\bigg|_0 w^i. \tag{11}$$

Evaluating the derivatives, we find

$$F_{ijk} = z^k C_{ijk}(\alpha, r) + z'^k C_{ijk}(\beta, r') + n_{ijk} m\lambda, \tag{12}$$

where $n_{ijk} = 0$ $(j,k \neq 0)$ and the n_{i00} are given up to sixth order in Table IV.

C. Location of the Gaussian image point

So far we have been making a purely geometrical calculation of the path F for two *arbitrary* points A and B. We now proceed to apply Fermat's principle to determine the actual direction of the outgoing beam. First consider the incoming principal ray AO. If this ray is to follow the path AOB_0 to the Gaussian image point $B_0 = (r_0', \beta_0, z_0')$, then Fermat's principle requires

$$\left.\frac{\partial F}{\partial w}\right|_{w=0,l=0} = 0, \quad \left.\frac{\partial F}{\partial l}\right|_{w=0,l=0} = 0. \tag{13}$$

This effectively sets the coefficients of the linear terms $(F_{100}$ and $F_{011})$ equal to zero, which implies

$$\frac{m\lambda}{d_0} = \sin\alpha + \sin\beta_0, \quad \frac{z}{r} + \frac{z_0'}{r_0'} = 0, \tag{14}$$

giving the grating equation and the law of magnification in the sagittal direction and thence the direction of the outgoing principal ray. To find the tangential focal distance r_0', we set the focusing term F_{200} equal to zero.

$$T(r,\alpha) + T(r_0', \beta_0) = 0 \qquad \text{(Rowland)} \tag{15}$$

$$T(r,\alpha) + T(r_0', \beta_0) + \frac{m\lambda}{\lambda_0}\left\{T(r_C, \gamma) \pm T(r_D, \delta)\right\} = 0 \qquad \text{(holographic)} \tag{16}$$

$$T(r,\alpha) + T(r_0', \beta_0) - \frac{v_1 m\lambda}{d_0} = 0 \qquad \text{(variable line spacing)} \tag{17}$$

Equations (14)–(17) determine the Gaussian image point $B_0 = (r_0', \beta_0, z_0')$, and in combination with the sagittal focusing condition (F_{020}=0), describe the focusing properties of grating systems under the paraxial approximation.

D. Calculation of ray aberrations

In an aberrated system, the outgoing ray will arrive at the Gaussian image plane at a point B_R displaced from B_0 by the ray aberrations $\Delta y'$ and $\Delta z'$ (Fig. 1) which we would like to calculate [28]. To do so, consider a Gaussian reference sphere with center B_0 and radius $\Re$ ($< r_0'$), chosen so that the rays OB_0 and PB_R and the line PB_0 intersect the sphere at real points O′, Q, and Q′, respectively (Fig. 2). Let the tangent plane to the sphere at O′ be the exit pupil plane with pupil coordinates (Y, Z) parallel and perpendicular to the principal plane, respectively. The ray aberrations may then be found from Eq. (10) of paragraph 5.1 of the book by Born and Wolf [3].

$$\Delta y' = \Re \frac{\partial \Phi}{\partial Y}, \quad \Delta z' = \Re \frac{\partial \Phi}{\partial Z} \tag{18}$$

In this equation, Φ is the "wave aberration function" [3], which is defined as the ray path length between the actual wave front and the Gaussian reference sphere when they instantaneously coincide at O′. We may calculate Φ as follows:

$$\begin{aligned} \Phi &= \mathrm{APQ} - \mathrm{AP\overline{Q}} \\ &\cong \mathrm{APQ'} - \mathrm{AP\overline{Q}} \\ &= \mathrm{APB_0} - \Re - \mathrm{AP\overline{Q}} \end{aligned} \tag{19}$$

where $\overline{Q}$ is the point where the ray PB_R intersects the wave front. Now $AP\overline{Q}$ is a constant (by the definition of a wave front), $\Re$ is a constant, and we have approximated the ray length PQ with the known length PQ′ measured along the line PB_0 (Eq. 7.8 of Welford 1974 [56]). We also know that when the position of P(ξ, w, l) is allowed to vary, the increments in the coordinates (Y, Z) of Q′ are given by $dY = dw \cos\beta_0 (\Re / r_0')$ and $dZ = dl(\Re / r_0')$. Therefore, the derivatives of Φ with respect to the coordinates of Q′ in Eq. (18) can be replaced by derivatives of F with respect to the coordinates of P as follows:

$$\Delta y' = \frac{r_0'}{\cos\beta_0} \frac{\partial F}{\partial w}, \quad \Delta z' = r_0' \frac{\partial F}{\partial l} \tag{20}$$

where F is to be evaluated at $A = (r, \alpha, z)$, $B = (r_0', \beta_0, z_0')$. From this development, one can see that the function F is related to the characteristic function (V) of Hamilton [3, 4, 56] but is not identical to it because specification of V requires a knowledge of the ray path whereas specification of F does not.

The importance of Eq. 20 is that, by means of the expansion of F, it allows the ray aberrations to be calculated separately for each aberration type. This is very useful for optical design and for understanding the results of exact ray tracing. Thus we have the equations

$$\Delta y'_{ijk} = \frac{r'_0}{\cos\beta_0}\frac{\partial}{\partial w}\left\{F_{ijk}w^i l^j\right\}, \quad \Delta z'_{ijk} = r'_0\frac{\partial}{\partial l}\left\{F_{ijk}w^i l^j\right\}. \tag{21}$$

Since the coefficients F_{ijk} are independent of w and l, the only way that an aberration can vanish when P is not at the origin is for its F_{ijk} to vanish. This is the justification for our use of F_{200}=0 to determine the focal distance in Eqs. (16)–(18). Moreover, provided the aberrations are not too large, they are additive;

$$\Delta y' = \sum_{ijk}\Delta y'_{ijk}, \quad \Delta z' = \sum_{ijk}\Delta z'_{ijk}, \tag{22}$$

implying that aberrations may either add or cancel (see section III).

E. The astigmatic curvature of focal lines

As an illustration of some of the principles described above, we calculate the largest resolution-determining aberration of the grazing-incidence toroid. Such a surface has steep sagittal curvature, which typically leads to a strong curvature $\Delta y' = k\Delta z'^2$ of the tangential focal line. Such line curvature, termed "astigmatic curvature" by Beutler [2], is an important consideration in the design of toroidal condensing mirrors and in determining the resolution of toroidal grating monochromators (TGM's). To understand it we note first that from Eq. (21) the astigmatism is given by

$$\Delta z'_{020} = r'\frac{\partial}{\partial l}\left\{F_{020}l^2\right\} = r'l(S+S'), \tag{23}$$

so we need those terms that give a $\Delta y'$ proportional to $\Delta z'^2$ after we have taken the derivative with respect to w and substituted for l from Eq. (23). There are three such terms [55]

$$\Delta y'_{lc} = \frac{r'}{\cos\alpha}\frac{\partial}{\partial w}\left(\frac{1}{2}wl^2F_{120} + wlF_{111} + wF_{102}\right) \tag{24}$$

all of which are non zero even though z=0. Making the substitutions for l and the F's and noting that, for the case at hand, a_{12}=0 and $\Delta z' = z'$, we get

$$\Delta y'_{lc} = \frac{\Delta z'^2}{2r'\cos\beta(S+S')^2}\left[\frac{S\sin\alpha}{r} + \frac{S'\sin\beta}{r'} - \frac{2(S+S')\sin\beta}{r'} + (S+S')^2\sin\beta\right]. \quad (25)$$

This equation can be applied to mirrors (α=$-\beta$), and it shows [16] that the line curvature vanishes if the imaging is stigmatic with unity magnification or if the tangential and sagittal magnifications are related by $M_s = 2M_t(1+M_t)$. For a grating system, Eq. (25) allows an estimate of the blurring of the spectral resolution resulting from curvature of the focal line. If the toroid is close to stigmatic, i.e., z and $z' \approx 0$, the F_{111} and F_{102} terms in Eq. (24) vanish and $\Delta y'_{lc}$ is determined mostly by the F_{120} aberration, which is large and dominates the spread function. If we now evaluate $\Delta y'_{lc}$ [14] as the sagittal curvature of the toroid is gradually reduced so as to progress from a stigmatic toroid toward a sphere, we see that the resolution broadening due to line curvature diminishes due to increasing cancellation among the three terms. By the time the toroid becomes a sphere, the line curvature contribution to the resolution becomes negligible for long-radius soft-x-ray systems and much reduced for shorter-radius VUV systems. This process is illustrated for a soft x-ray TGM/SGM in Fig. 3. As shown in the figure, these conclusions are confirmed by ray tracing, and they provide an explanation for the superiority of the resolution of monochromators with long-radius spherical gratings [50] compared to their toroidal predecessors.

III. Application of aberration theory to the design of an undulator-based SGM

A. General design principles

To illustrate the design concepts described in the previous section, we have chosen to examine in detail the design adopted for an existing undulator beamline at the ALS. This beamline, 9.0.1, has a 4.5-m-long, 10-cm-period undulator source; a Kirkpatrick–Baez condenser system, focused on the entrance slit in the vertical plane and the sample in the horizontal plane; and a spherical-grating monochromator. This monochromator system [5, 6, 14, 31] was first demonstrated by Chen and Sette in 1986 and has since become one of the standard types. The basic system has a fixed entrance slit, a spherical grating with a fixed rotation axis, and an exit slit. The grating-to-exit-slit distance can be varied to achieve focus, but the included angle (2θ) at the grating is fixed. The beamline 9.0.1 instrument uses three interchangeable gratings to cover the energy range from 20–300 eV [12]. It is used for atomic and molecular spectroscopy and was

designed so that high resolution could be achieved while still maintaining good throughput. The system has the following basic parameters:

entrance arm length, r	1.45 m
exit arm length, r'	4.02–4.78 m
included angle, 2θ	165°
grating groove density, $1/d_0$	380, 925, 2100 /mm
diffraction order, m	+1
grating radius, R	21 m
vertical demagnification, source-to-slit	8.04:1
horizontal demagnification, source-to-sample	1:1

We will now examine how these parameters were derived, using the value of the minimum wavelength $(\lambda_{\min})$ as a stating point. The first choice to be made is that of the overall size of the monochromator. This should be as large as space allows for maximum phase-space acceptance of the instrument. In the case at hand, the length from entrance to exit slit, was set at 6 m.

The included angle of the monochromator is determined by requiring adequate reflectivity at angle θ (not α) at the highest intended photon energy. In the present case, using a nickel coating for the lowest-wavelength grating, reasonable reflectivity (~ 45% at 300 eV) is obtained at an included angle of 165°.

Given the slit-to-slit length (AB_0) of the instrument (see Fig. 1) and the complement θ_G of θ, one can make a good estimate of the grating radius R, which plays the role of an overall scale factor for the system. From a diagram of the Rowland circle and the principal ray AOB_0, we find $AB_0 \approx 2\theta_G R$. To make further progress we use the grating equation [Eq. (14)] and by taking derivatives we can obtain the following useful quantities: the reciprocal linear dispersion $d\lambda / d(\Delta y')$, the entrance- and exit-slit-width-limited resolution and the horizon wavelength λ_H (at which either α or β equals 90°):

$$\frac{d\lambda}{d(\Delta y')} = \frac{d_0 \cos\beta}{mr'} \qquad \Delta\lambda|_{ent} = \frac{s d_0 \cos\alpha}{mr} \qquad \Delta\lambda|_{exit} = \frac{s' d_0 \cos\beta}{mr'} \qquad \lambda_H = 2d_0 \cos^2\theta , \tag{26}$$

where s and s' are the entrance and exit slit widths.

To analyze the focusing conditions, we first consider the Rowland solution, in which the two terms of Eq. (15) are set separately equal to zero, leading to $r = R\cos\alpha$, $r' = R\cos\beta$. We will not generally be using this solution in the case of an SGM because r' will be constantly changing to achieve focus. However, it can be shown that the value of r' needed for focus has a stationary point that occurs approximately at the Rowland wavelength (λ_R), and therefore the amount of slit travel can be minimized by setting λ_R at the center of the wavelength range. Adopting this condition then allows us to choose values for r and r'. However, it turns out that, even with the help of the stationary point, we can still only build the r' motion to cover about a factor of 2.5 in wavelength. This fact completes our definition of the wavelength range and the entire monochromator geometry for the lowest-wavelength grating except for the groove density to which we now turn.

The choice of groove density depends on the resolution requirement, and there are two main possibilities:

(i) the best possible resolution capability at the minimum practical slit widths,

(ii) the maximum flux at some particular value of the resolution.

The latter requirement applies especially to monochromators dedicated to a single application and is similar to the needs of microscopy beamlines which are discussed in a later section. For the best resolution, the groove density should be maximized, which means that it will be limited by the horizon effect according to

$$3.5\lambda_{min} \approx 0.8\lambda_H = 1.6 d_0 \cos^2\theta. \qquad (27)$$

The maximum flux (i.e., the maximum grating efficiency) requires the *minimum* groove density as discussed later. The phase-space acceptance of an SGM is given by $N\Delta\lambda|_{ent}$ [14] where N is the number of illuminated grooves. Thus, given a grating of the largest practical size, reducing the groove density at fixed resolution amounts to a reduction of the phase-space acceptance. This will still be advantageous (for flux) until the incoming beam emittance is matched. Thus, the groove density should be chosen to achieve a phase-space match or, if that is impossible, the choice should revert to Eq. (29).

Having thus obtained a candidate design for the lowest wavelength grating we can obtain a design for the next one by scaling up the groove width by a factor 2.5 so that $m\lambda/d_0$ will be unchanged. All the design parameters will then be the same as for the lowest-wavelength grating as will also the resolving power. According to the 2.5× multiplication rule, our present example would then have three wavelength ranges 40-100, 100-250 and 250-625 Å

B. Calculation of the effect of grating aberrations on energy resolution.

We have shown in a previous section how individual terms of the optical path function can be associated with aberrations that scale with powers of the ray coordinates on the grating, w and l. In addition, Eq. (21) shows how these terms can be related directly to the ray aberrations at an image plane. Combining this with the dispersion given by Eq. (28), we can calculate the effect in terms of a deviation (ΔE) from the nominal photon energy registered by the principal ray. The most important wavelength aberrations in SGMs are F_{200} (defocus), F_{300} (aperture defect or coma) and F_{400} (spherical aberration). As previously shown, the astigmatic curvature [Eq. (25)], although dominant in toroidal grating monochromators, is usually small in SGMs.

Taking a grating of length 150 m and width 44 mm, Fig. 4 shows the contributions from all the above aberrations for $w = w_{\max}$, $l = l_{\max}$ and their sum at photon energies from 40–120 eV, with a *fixed* exit arm length r' of 4.4 m. The same thing is shown in Fig. 5 except that r' has been set for focus. This also brings about consequential changes in aberrations other than defocus, including a shift of the coma zero. Note that, in both these plots, the spherical aberration and line curvature terms are scaled by 10× and 1000×, respectively. The defocus curve goes through two zeroes, as expected, and the coma curve goes through one. The spherical aberration is small and always positive, and the line curvature, as expected, is negligibly small (see section II). The individual aberrations are shown in their signed form, meaning that the signs are those of the aberration coefficients, $w_{\max}$ and $l_{\max}$ being positive. In this way we can see how the individual components may be summed. Defocus and spherical aberration scale as odd powers of w, so they change sign when w goes negative. Coma, on the other hand, scales as w^2 and therefore always has the sign of the coefficient. Representing defocus, coma, and spherical aberration by d, c, and s respectively, we obtain the full-width-at-zero-height value of ΔE by looking for the maximum algebraic difference among $(d + c + s)$, (0), and $(-d + c - s)$. An interesting effect of this algebraic differencing can be seen in the region greater than 83 eV, where defocus is negative but becoming smaller and coma is positive and becoming larger. At 115 eV, the coma equals the sum of defocus and spherical aberration. For photon energies less than this, the extreme rays are given by $(d + c + s)$ and $(-d + c - s)$, and for those greater, they are given by $(d + c + s)$ and (0). The result is the jump in the rate of change of aberration at 115 eV as one half of the defocus is eliminated. This effect is typical of the analysis based only on the principal ray and the two marginal rays. A more complete analysis would include all the rays, and we examine this in more detail in the next section.

C. Calculation of spectral lineshapes

The calculation of aberrations in terms of the principal and marginal rays gives an approximate understanding of the magnitude of the error and is useful in performing fast optimizations. However, for a detailed understanding of the resolution of a system, we must calculate the spectral lineshape. This can be done by applying the method previously outlined to a distribution of points across the grating surface. Fig. 6 shows the photon energy errors resulting from individual aberration terms as a function of the w coordinate (Fig. 1) for a fixed exit arm length of 4.133 m at a photon energy of 100 eV. This shows that, for the negative side of the grating, defocus and coma subtract, and on the positive side they add. Combined with a small spherical aberration term, the net effect (dashed curve) is to produce a small negative aberration on the negative side and a large positive one on the positive side.

The information plotted in Fig. 6 allows us to predict spectral lineshapes. If we draw a horizontal line at a particular ΔE value in Fig. 6, it could cross the summed curve at up to three locations. Each of these will correspond to a position, w, on the grating, illuminated with a local photon flux per unit width, $I(w)$ (say). The flux per unit energy range $di/d(\Delta E)$ in the image plane therefore depends on $I(w)$ at the w values of the crossing points and also on the gradient $\partial w/\partial(\Delta E)$ in Fig. 6. For example, in the case of pure coma, the calculation proceeds as follows.

$$\Delta y'_{300} = \frac{r'_0}{\cos\beta_0} 3w^2 F_{300} \quad \text{(by Eq. 21).}$$

$$\frac{d\lambda}{d(\Delta y')} = \frac{d_0 \cos\beta_0}{m r'_0} \quad \text{(by Eq. 28).}$$

$$|\Delta E| = \frac{hc\Delta\lambda}{\lambda^2}, \quad \text{so that} \quad |\Delta E_{300}| = \frac{3hcd_0F_{300}}{m\lambda^2} w^2. \tag{28}$$

$$\frac{di}{d(\Delta E_{300})} = \frac{di}{dw}\frac{dw}{d(\Delta E_{300})} = \frac{I(w)}{2}\sqrt{\frac{m\lambda^2}{3hcd_0F_{300}}}\frac{1}{\sqrt{|\Delta E_{300}|}}.$$

For a uniformly illuminated grating ($I(w)$=constant), the intensity in the image plane due to coma will thus be proportional to $1/\sqrt{\Delta E}$, and the intensity will be infinite on axis and have long tails. Also from Fig. 6, it is clear that we should expect steps in intensity, corresponding to the ends of the summed curve, for example at around -3 meV, where the right-hand part of the summed curve reaches the edge of the grating.

These effects can be seen in Fig. 7, where the same case of 100 eV is used, but the lineshapes have been assessed for exit-arm lengths of 4.113–4.193 m in steps of 0.02 m. Curve (e) (4.193 m) corresponds to the in-focus condition, and we can see its expected single-sided distribution (due to the fact that the dominant aberration, which is coma, scales with an even power of w), and the asymptotic rise in the gradient $\partial w / \partial(\Delta E)$ as ΔE approaches its minimum value. We can also see steps in intensity at +65 and +79 meV. From Fig. 6, we can see that the maximum coma (with a slightly different exit-arm length) is 71 meV, and the maximum spherical aberration is ±7 meV. The negative-w end of the grating therefore will have a maximum error of 64 meV, and the positive-w end, 78 meV. We can therefore associate the two steps with the total aberration for the extreme rays on the grating. If we look at curve (b) in Fig. 7, which is the $r' = 4.133$ m curve (previously described in Fig. 6), we see that the features can be easily correlated. The asymptotic limit is at -17 meV, corresponding to the minimum in the sum curve of Fig. 6, and there are sharp breaks at -3 meV and +144 meV corresponding to the endpoints of the sum curve at the edges of the grating.

The case of Fig. 7 would correspond to an overfilled grating, a situation that is common on bending magnet beamlines. To simulate an undulator source, we have to take into account the narrow angular divergence of the source and diffraction from the entrance slits. In the case shown in Fig. 5, we have taken a 4.5-m undulator, radiating at 100 eV, a demagnification 8:1 onto an entrance slit of width 10 μm. We have approximated the two angular distributions due to the undulator and the slit by their gaussian equivalents.

$$\sigma_u = \sqrt{\frac{\lambda}{L}}, \quad \sigma_s = \frac{\lambda}{2s}, \quad I(w) = Are^{-\frac{w^2}{2\Sigma^2}}, \quad \Sigma^2 = \sigma_u^2 + \sigma_s^2 \tag{29}$$

where L is the length of the undulator and we have neglected the effect of the vertical electron beam divergence. In this case, Fig. 8 shows the resulting intensity distribution for r'=4.133–4.193-m exit-arm lengths in 0.02-m steps, this time for the more highly-localized undulator radiation. We can see some remarkable differences between the two cases of uniform illumination and radiation from an undulator. The most striking is that the steps evident in Fig. 7 have disappeared and that, when significantly out of focus (4.133 m), the asymptote disappears. The reason for both is that the undulator beam is illuminating a region near the center of the grating, and so the termination of the $di/d(\Delta E)$-versus-ΔE curve happens smoothly because the intensity falls to zero smoothly. In addition, near the center the dominant aberration is defocus, which is seen as a slow intensity variation. The absence of the asymptotic cusp is due to the fact that there is no intensity at the

minimum of the ΔE curve at w=-37 mm (curve (d), Fig. 6).

The inclusion of slit diffraction is critical if an accurate estimate of the spectral line shape is to be made. The same effect guarantees (via the van Cittert–Zernike theorem) to coherently illuminate the appropriate number of grooves N_0 on the grating to produce the calculated slit-width-limited resolution and the diffraction-limited resolution mN_0, which are now seen to be the same. We show the effect of slit width on line shape in Fig. 9 for slit sizes of 2 μm, 6 μm, 10 μm, 25 μm and fully open for a photon energy of 64 eV and for the in-focus condition. We have chosen this energy because extensive studies of the double-ionization series of helium have been conducted in this region, and in particular, recent work by Kaindl and collaborators [50], using the SGM on ALS beam-line 9.0.1 that we have been studying, has demonstrated a resolution of 65000 at this energy. The helium spectrum in question is given in Fig. 10, which shows the extraordinary resolving power achieved. The 2p3d peak at 64.117 eV is particularly interesting as it has a natural linewidth of a few μeV, so that what we see is the real lineshape function.

It can be seen from Fig. 9 that the calculated aberration-limited line width broadens as the slits are closed. This occurs because the divergence of the light increases as the slit is closed, filling more of the grating and increasing all of the aberrations. In order to make a fair comparison of line shapes, we clearly cannot take the peak height into account, as the distribution on axis would go to infinity and is only prevented here by the finite sampling. However, the integral is finite, and so we take the 50% integral point from the asymptotic cusp as a measure of the width, and the data are normalized to that value. We therefore arrive at aberration-limited widths of 2.1, 1.1, 0.67, 0.23, and 0.13 meV for the 2-μm, 6-μm, 10-μm, 25-μm, and open slit cases. (the demagnified undulator source geometry is used for the latter). The corresponding slit-width-limited resolutions are 0.3, 0.9, 1.5, and 3.8 meV for the 2-μm, 6-μm, 10-μm, and 25-μm slit openings. Combining the slit and aberration limits indicates an optimum around 6 μm slit width which is in reasonable agreement with the measured resolution of 1 meV. Moreover, it is clear from the shape of the experimental curve that the broadening is due to residual coma. Note also that the sign of the coma aberration is the same in the experimental and theoretical curves at 64 eV but reversed from the curve at 100 eV. This is because the sign of the coma changes at the coma zero, which is at 71 eV (Fig 5). In the theoretical curves, also note that for the smallest slit size, sufficient intensity is diffracted to the edge of the grating that the sharp truncations of the coma and spherical aberration again become apparent.

Geometrical aberration theory can therefore be used at several different levels. On the one hand, it can be rapidly used to assess gross performance by prediction of the extreme ray aberrations. On

the other hand, it can be used to predict line shapes in a more precise way. In this sense, grating aberration theory is a powerful tool for understanding design possibilities and arriving at candidate designs. Once a design is established, it is useful to run a ray trace from a point source with only a few rays positioned on a regular grid. (The SHADOW code [22] maintained by the Center for X-ray Lithography at the University of Wisconsin is the one most suited for synchrotron-radiation applications.) One should be able to explain quantitatively why every ray goes where it does on the basis of the aberration calculations from Eq. (21) and observations such as the relative positions of the rays from w_{max} and $w_{max}/2$, etc. Once a candidate design that meets requirements has been established, it then becomes useful to run SHADOW again, this time with a realistic source and a larger number of rays to verify the correctness of the design and to study other aspects of it.

IV. Focusing in variable-included-angle monochromators

In the previous section, we showed how grating aberration theory could be applied to a fixed-deviation-angle SGM to extract information on focusing, aberrations, and line shapes. The same approach can also be applied to other monochromators, where there is a single focusing element, including the case where a movable plane mirror is used to vary the included angle at the grating. Two such cases are the variable-included-angle SGM [18, 22, 32, 36] and the SX700 [38, 39, 41]. In these monochromators, the included angle becomes a user-controlled variable and not only determines focusing, but also modifies the efficiency behavior of the system.

We have seen how it is possible in a fixed-deviation-angle SGM to keep the defocus term zero by moving the exit slits. Sometimes, particularly in microscopy where the microscope optics are fixed, the exit slit has to be in a fixed location. The variable-angle SGM achieves focus at fixed r and r', i.e., with fixed slits, by varying the included angle. According to Eq. (15) with $a_{20} = 1/2R$, the condition for focus is

$$\frac{\cos^2\alpha}{r^*} - \cos\alpha + \frac{\cos^2\beta}{r'^*} - \cos\beta = 0 \tag{30}$$

where $r^* = r/R$, $r'^* = r'/R$. If α is regarded as the independent variable, then this equation can be solved for β as a function of α. Then, using the sign convention defined in section II, the included angle, 2θ, is obtained as α–β. For each α/β pair, the grating equation yields the wavelength, and we can plot included angle against photon energy (Fig. 11). By selecting differing

grating radii, we can then select different solutions with different angles while keeping r and r' constant. Three different solutions are illustrated in Fig. 11. The action of changing the grating radius causes the focusing curve to be moved on both the energy scale and the included-angle scale. The figure shows curves for both solutions to the quadratic, which join at the low-energy limit, although only the lower solution has practical value. Changing the radius has the desirable effect that the mean included angle can be set to a value appropriate for the energy ranges of each separate grating. This is advantageous for collection aperture, order sorting, and, as we will see in the next section, for diffraction efficiency. However, Fig. 11 shows that the amount of change in the angle within the scan range of any one grating is always small (about a degree or less). On the other hand, if we want to optimize diffraction efficiency, say for a rectangular phase grating in mth order, then the path length difference between rays diffracted at the top and bottom of the grooves has to be m wavelengths. Therefore the included half-angle θ should vary roughly as $\theta = \cos^{-1}(m\lambda/2h)$, where h is the groove depth, whereas in fact, as Fig. 11 shows, it must be kept roughly constant to hold focus. The variable-angle SGM thus allows us to have a fixed exit slit and optimum efficiency at one wavelength for each grating, but it still has the problem of the standard SGM; it has a limited tuning range per grating and still cannot track the diffraction efficiency maximum.

These disadvantages are overcome to a considerable degree in the SX700 system originally proposed by Petersen in 1980 [38, 39, 41]. It was the first instrument to use included-angle control by means of a plane mirror and this was combined with a plane grating and fixed focusing mirror. The latter was originally an ellipsoid of revolution, but in later instruments that was superseded by a more-easily-manufactured spherical mirror [32, 44]. The astigmatism of the spherical mirror at grazing incidence was overcome using a separate mirror outside the monochromator focusing in the non-dispersive direction, and the coma of the sphere was reduced sufficiently by selecting an appropriate magnification.

The focusing condition of the monochromator is given by Eq. (30) with R equal to infinity.

$$r' = -r\frac{\cos^2\beta}{\cos^2\alpha} = -rC^2 \tag{31}$$

We can see that a virtual image is formed at a distance rC^2 behind the grating. The function of the plane premirror in this design is again to select an included angle that will maintain focus. Other operational modes of the monochromator are possible with different included angles, at the expense of no longer being in focus, for example to reduce harmonics or to exactly track the

efficiency maximum. In a later version of the system, moveable exit slits were used so that, for an entrance-slitless version of the monochromator, a larger value of α could be used to improve the source-size-limited resolution at the expense of flux. If α is eliminated between Eq. (31) and the grating equation, we obtain

$$1-\left(\frac{m\lambda}{d_0}-\sin\beta\right)^2=\frac{\cos^2\beta}{C^2} \quad \text{or} \quad \sin\beta=\frac{\frac{m\lambda}{d_0}-\sqrt{\left(1-C^{-2}\right)^2+\left(\frac{m\lambda}{Cd_0}\right)^2}}{1-C^{-2}}. \tag{32}$$

Three solutions are shown in Fig. 12. One can see that, unlike the SGM and variable-angle SGM, a wide range of both wavelength and included angle is spanned for a single grating. In addition, the curve strongly decreases as the photon energy decreases, as required for maximizing diffraction efficiency.

V. Diffraction efficiency

One starting point for a monochromator design is to know the maximum diffraction efficiency that can be obtained at a particular photon energy under optimum conditions. In principle this would need many time-consuming calculations, but a range of these have been done by Padmore et al. [34] for gold- and nickel-coated rectangular phase gratings from 300 to 1200 /mm and from 100 to 2000 eV. These provide values of the maximum possible efficiency and the deviation angle, groove depth, and groove width necessary to get it for each line density and energy. The calculated results were shown to agree with both experiment and reciprocity. Maximum efficiency can vary significantly, depending on line density. For example, a 300 /mm grating at 1500 eV has a diffraction efficiency maximum of 33% for a deviation angle of 178°. For a 1200 /mm grating, the maximum efficiency is 8% for a deviation angle of 176°. The tendency is always for the diffraction efficiency and the optimum deviation angle to decrease at high line density. For the present purpose the diffraction process is best described in terms of the *deviation* angle because this is the most directly related to the important physical quantity, which is the momentum transfer.

To illustrate the characterization of grating efficiency for particular geometries, we have chosen the SX700 case. Fig. 13 shows the "nomogram" for a 1200 /mm gold-coated grating. The upper panel gives the maximum diffraction efficiency; the middle panel, the required deviation angle; and the lower panel, the required groove depth and width. The figure shows two cases, one

(dotted) in which the deviation angle, groove width, and groove depth are variable parameters, and one in which the deviation angle is constrained to the SX700 fixed-focus condition for the same groove parameters. It can be seen that the two curves are virtually identical. It can also be seen that the diffraction efficiency is above 10% from 100 to 1400 eV, dropping only to 6% at 2 keV. Of course, having continuously variable groove parameters is not realizable in practice, and Fig. 14 shows what happens when they are fixed. The groove depth and width have been optimized at 500 eV, and it can be seen that only at energies less than 300 eV is there significant variance between the fully optimized case and the case with fixed groove parameters.

The SX700 geometry therefore offers the enormous advantage of staying always close to the blaze-maximum condition. In addition, if we allow ourselves the possibility to have more than one groove depth and width, then we can have optimized performance in the region below 300 eV. This can be done in practice by having either more than one grating or more than one ruling on a single grating.

We have presented the case above where a monochromator has to tune over a very wide energy region. There are many cases where this is unnecessary, and we are increasingly designing for highly specific experiments where simpler monochromator systems can be used. However, the starting point is still to understand the relationship between deviation angle and efficiency, using the tabulations described above.

VI. An optimized beam line for microscopy by X-PEEM and micro-XPS

To illustrate some of the issues of monochromator design, and to show some of the special considerations necessary when designing systems for microscopes, we will describe beam line 7.3.1 at the ALS. The layout of the beam line is given in Fig. 15 [34, 35]. The system was originally designed for Photoelectron Emission Microscopy (X-PEEM), applied to the study of magnetic materials. The materials of interest, the upper 3d transition metals (2p–3d edges) and up to the middle of the rare earths (3d–4f edges) have a relatively narrow band of energies from around 650 eV to 1300 eV. The PEEM itself requires an illuminated field of view of about 30 μm with maximum flux density. As the PEEM selects its own field of view, it can also act as an effective exit slit. Thus, considering the vertical source size of around 30 μm FWHM, we chose to build a single-grating fixed-angle SGM in entrance- and exit-slitless mode at 1:1 monochromatic magnification. As the core-level widths of the edges we wished to study were rather large, we also designed the system to have a deliberately moderate resolution. By making the instrument

sufficiently long, a very low line density grating (200 /mm) could be used. This combined with the relatively small energy range and the resulting small change of focal length with energy meant that we could operate with fixed exit slits, or in this case, with a fixed sample. The use of such a low line density also has the added advantage that the diffraction efficiency is very high, typically 30% at 1 keV.

In the horizontal direction, the object was to collect as much light as possible and condense it to the field size of 30 μm. We have a horizontal source size of around 300 μm FWHM, so an illumination width of 30 μm requires a demagnification of 10. The maximum angular spread that can be passed by the horizontal condenser mirror is about half the critical angle at the maximum photon energy. At 1.3 keV, this means a maximum of 25 mrads convergence, or 2.5 mrads collection from the source. The resulting elliptical-cylinder condenser mirror is particularly challenging. It is 1 m in length and requires an rms slope error tolerance of 3 μrads to preserve the source brightness as well as a superfine finish. A rigid mirror of this specification is beyond the state of the art, and we have adopted a method based on bending of a flat plate with specially calculated width variation. This beamline is predicted to give a flux of 3×10^{12} ph/sec in a 0.5 eV bandpass at 1 keV in a 30-μm-diameter spot size.

The application-specific nature of the beamline, together with the need to have the maximum flux density in the field of the PEEM, has led us to a unique design that is both highly efficient and much simpler than that of a traditional beamline. Due to the special needs of x-ray microscopy and of the materials issues that are being addressed with the new generation of microscopes, there are likely to be more systems of this type—highly specific to one task, highly optimized, but simplified by removing the demand for universal capabilities. The exact matching of the system to a particular function also tends to imply exclusive use of the beamline by a single user group, and such an arrangement can normally be considered only on a bending magnet.

A further example of this approach is given by a branch of the same beamline. This branch splits off 0.2 mrads of horizontal aperture from the X-PEEM beamline using a horizontally deflecting mirror. This produces a 2:1 demagnified image of the horizontal source at the monochromatic focal plane of the monochromator. At this location, we have a pair of bilaterally adjustable slits that define the source for the microscope that follows. The nominal setting is 20 μm vertical by 40 μm horizontal. The horizontal image of the ALS is 150 μm wide at this location, so the slits are significantly overfilled. We can now apply the same phase-space arguments as for X-PEEM, but in this case we wish to demagnify to a 1-μm spot size, and we use a slightly smaller grazing angle of 1.6° on the probe-forming optics. These are a Kirkpatrick–Baez pair, again

elliptical and produced by the bending of width-profiled flats by the application of unequal couples [33]. The vertical demagnification is 20:1, and using our half-critical-angle rule, we derive a convergence angle of 12 mrads. This means that we have an acceptance from the source of 0.6 mrads in the vertical direction. This value is approximately equal to the divergence of the light from the source at 1 keV. We can therefore say that, in the vertical direction, light from an ALS bending magnet can be focused by a mirror operating at 1 keV to an image size of 1 μm without geometric loss. In the horizontal direction, the convergence onto the sample is the same, 12 mrads, but the demagnification is 40:1. The acceptance from the source is therefore 0.15 mrads, with a loss of a factor of 4 in throughput at the horizontally defining slits. Even so, the predicted (and measured) flux in the focused spot is 3×10^{10} ph/sec in the so-far-achieved spot size of 2×2 μm^2, with a 0.5 eV bandpass. This is sufficient for x-ray photoelectron spectroscopy (XPS) using modern high-aperture analyzers with multichannel detection. In the present case, the system was developed for the microelectronics industry, specifically to perform scanning micro-XPS on large-area (50-mm-diameter) samples. It was important to design a system that was economical and had sufficient flux at its design resolution to enable a high throughput of samples.

It can be seen from the above examples that the design of monochromators to be used in conjunction with microscopes is significantly different from that for high-resolution spectroscopy. Wherever possible, these optical systems should be separated, as they clearly have very different design constraints and lead to very different optimized solutions.

Acknowledgements

This work was supported by the Director, Office of Energy Research, Office of Basic Energy Sciences, Materials Sciences Division of the U.S. Department of Energy, under Contract no. DE-AC03-76SF00098.

Figure Captions

1. Geometry and notation for grating theory. The axes and the rays are represented by continuous lines and other distances by broken lines.

2. Geometry for calculation of the wavefront aberration function and the definition of the points Q, Q' and $\overline{Q}$. PB_R represents the ray and B_0 the Gaussian image point.

3. Relation of the energy resolution of a soft x-ray toroidal grating monochromator to the minor radius of the grating and thus to the curvature of the focal line. Parameters: included angle=174°, d_0^{-1}=1100/mm, λ=20Å, R=55m, arm lengths: set to satisfy the Rowland condition.

4. Aberration components and their sum are shown for the 9.0.1 SGM with a fixed exit arm length r' of 4.4 m, and a ruled length and width of 150 and 44 mm. Defocus is shown by the small dashes, coma by the medium dashes, spherical aberration ×10 by the large dashes and line curvature ×1000 by the extra-large. The sum is shown by the solid line.

5. Aberration components and their sum are shown with the exit arm set to eliminate defocus and a ruled length and width of 150 and 44 mm. Coma is shown by the small dashes, spherical aberration by the medium dashes and the entrance- and exit-slit-limited resolution for 10 μm slits by the large and extra-large dashes respectively. The sum is shown by the solid line.

6. Aberration components are shown as a function of position in the w direction on the grating, with l=0, for an exit arm length r' of 4.133 m and a photon energy of 100 eV. Defocus, coma, spherical aberration and the sum are indicated by a, b, c and d respectively.

7. The spectral distribution is shown for a photon energy of 100 eV, with a uniformly illuminated grating with a length of 150 mm and a width of 44 mm. Distributions are shown for exit arm lengths r' of 4.113 (a), 4.133 (b), 4.153 (c), 4.173 (d) and 4.193 (e). The latter case is in focus.

8. The spectral distribution is shown for a photon energy of 100 eV, with a grating of length 150 mm and width 44 mm illuminated by an undulator source. The undulator is 4.5 m in length, 8:1 demagnification from the source to slit is used and diffraction is included for 10

μm slits. Distributions are shown for exit arm lengths r' equal to 4.193 (a), 4.173 (b), 4.153 (c) and 4.113 (d). The case (a) is in focus.

9. The spectral distribution is shown for 64 eV, undulator illumination, and for entrance slit sizes of 2, 6, 10, 25 μm and fully open. 2 μm corresponds to the widest distribution. The horizontal line gives the 50% integral point for each curve, yielding widths of 2.1, 1.1, 0.67, 0.23 and 0.13 meV for the above slit sizes.

10. The double ionization series of helium is shown near the ionization limit of the + series. The 2p3d feature has a natural linewidth of a few μeV, and so the feature here should directly map the line shape function of the monochromator.

11. Three different solutions for a variable angle SGM with a 1200 /mm grating in positive first order: the values of r^* and r'^* are 0.1 and 0.2 (a), 0.05 and 0.1 (b), and 0.033 and 0.066 (c).

12. Three solutions of Eq. (33) for a 1200 /mm grating in +1 order with C values of 4.4 (a), 2.1 (b) and 1.45 (c).

13. Optimum efficiency of a 1200 /mm gold-coated grating and the deviation angle, groove depth and groove width needed to get it. For the dashed curve (best case), the deviation angle and groove depth and width are all varied in the search for an optimum while for the continuous curve the groove depth and width are the same but the deviation angle is chosen to focus an SX700 with C=2.166.

14. Similar to Fig. 13 except that the groove width and depth are fixed at the values needed for an optimum at 500 eV. The short-dash curve is for the best deviation angle while the continuous curve is for the angle that would focus an SX700 with C=2.094. The "best-case" curve of Fig. 13 is shown (long dash) for comparison.

15. Optical systems of ALS beam line 7.3.1 as discussed in the text

References

1. Abramson, N., *J. Opt. Soc. Am. A*, **6**, 627-629 (1989).

2. Beutler, H. G., *J. Opt. Soc. Am.*, **35**, 311-350 (1945).

3. Born, M., E. Wolf, *Principles of Optics*, Pergamon, Oxford, 1980.

4. Buchdahl, H. A., *An Introduction to Hamiltonian Optics*, Cambridge University Press, Cambridge, 1970.

5. Chen, C. T., *Nucl. Instr. Meth.*, **A 256**, 595-604 (1987).

6. Chen, C. T., F. Sette, *Rev. Sci. Instrum.*, **60**, 1616 - 1621 (1989).

7. Ederer, D. L., J. B. West, ed., *Proc. Nat. Conf. Synchrotron Radiation Instrumentation*, Nucl. Instrum. Meth. 172 (1980), , 1979.

8. Gudat, W., C. Kunz, in Kunz, C., (Ed), Vol. **10**, Springer Series on Topics in Current Physics, Berlin, 1979.

9. Haber, H., *J. Opt. Soc. Am.*, **40**, 153-165 (1950).

10. Haensel, R., C. Kunz, *Z. Angew. Phys.*, **23**, 276 - 295 (1967).

11. Harada, T., T. Kita, *Appl. Opt.*, **19**, 3987-3993 (1980).

12. Heimann, P., T. Warwick, M. Howells, W. McKinney, D. DiGennaro, B. Gee, D. Yee, B. M. Kincaid, *Nucl. Instrum. Meth.*, **A319**, 106-109 (1992).

13. Hettrick, M. C., *Appl. Opt.*, **23**, 3221-3235 (1984).

14. Hogrefe, H., M. R. Howells, E. Hoyer, in *Soft X-ray Optics and Technology*, Koch, E.-E., G. Schmahl, (Ed), Proc. SPIE, Vol. **733**, SPIE, Bellingham, 1986.

15. Howells, M., in *Synchrotron Radiation Sources and Applications; Proceedings of the*

Thirtieth Scottish Universities Summer School in Physics (SUSSP), Aberdeen, Sept 1985, Greaves, G. N., I. H. Munro, (Eds), SUSSP, IOP Publishing (Adam Hilger), Edinburgh, 1989.

16. Howells, M. R., in *New Directions in Research with Third-Generation Soft X-ray Sources*, Schlachter, A. S., F. J. Wuilleumier, (Eds), Kluwer, London, 1994.

17. Hunter, W. R., in *Spectrometric Techniques*, Vol. **IV**, Academic Press, Orlando, 1985.

18. Jark, W., P. Melpignano, *Nucl. Instrum. Meth.*, **A349**, 263-268 (1994).

19. Johnson, R. L., *Handbook of Synchrotron Radiation , Vol 1A*, E. E. Koch (ed), North Holland, Amsterdam, 1983.

20. Koch, E. E., R. Haensel, C. Kunz, eds., *Proc. 4th Int. Conf. on Vacuum Ultraviolet Physics*, Hamburg, 1974.

21. Laberie, A., J. Flammand, *Opt. Comm.*, **1**, 5-8 (1969).

22. Lai, B., F. Cerrina, *Nucl. Instrum. Meth.*, **A246**, 337-341 (1986).

23. Mack, J. E., J. R. Stehn, B. Edlen, *J. Opt. Soc. Am.*, **22**, 245-264 (1932).

24. Madden, R. P., in *X-ray Spectroscopy*, Azaroff, L. V., (Ed), McGraw-Hill, New York, 1974.

25. Marr, G. V., I. H. Munro, (eds.), *International Symposium for Synchrotron Radiation Users*, Vol. DNPL/R26, Daresbury Nuclear Physics Laboratory, Daresbury, 1973.

26. McKinney, W. R., *Rev. Sci. Inst.*, **63**, 1410-1414 (1992).

27. Namioka, T., *J. Opt. Soc. Am.*, **51**, 4-12 (1961).

28. Namioka, T., M. Koike, *Nucl. Instrum. Meth.*, **A319**, 219-227 (1992).

29. Namioka, T., H. Noda, M. Seya, *Sci. Light*, **22**, 77-99 (1973).

30. Noda, H., T. Namioka, M. Seya, *J. Opt. Soc. Am.*, **64**, 1031-6 (1974).

31. Padmore, H. A., in *Soft X-ray Optics and Technology*, Koch, E.-E., G. Schmahl, (Eds), Proc. SPIE, Vol. **733**, 1986.

32. Padmore, H. A., *Rev. Sci. Instrum.*, **60**, 1608-1616 (1989).

33. Padmore, H. A., M. R. Howells, S. Irick, T. Renner, R. Sandler, Y.-M. Koo, in *Optics for High-Brightness Synchrotron Radiation Beam Lines II*, Arthur, (Ed), Proc. SPIE, Vol. **2856**, SPIE, Bellingham, 1996.

34. Padmore, H. A., T. Warwick, *J. Synch. Rad.*, **1**, 27-36 (1994).

35. Padmore, H. A., T. Warwick, *J. Electron. Spect.*, **75**, 9-22 (1995).

36. Peatman, W. B., J. Bahrdt, F. Eggenstein, G. Reichardt, F. Senf, *Rev. Sci. Inst.*, **66**, (1995).

37. Peatman, W. B., F. Senf, in *Vacuum Ultraviolet Radiation Physics (VUV11)*, Wuilleumier, F. J., Y. Petrof, I. Nenner, (Eds), World Scientific, Singapore, 1992.

38. Petersen, H., *Opt. Comm.*, **40**, 402-6 (1982).

39. Petersen, H., *Nucl. Inst. Meth.*, **A246**, 260-3 (1986).

40. Petersen, H., in *Soft X-ray Optics and Technology*, Koch, E. E., G. Schmahl, (Ed), Proc. SPIE., Vol. **733**, SPIE, Bellingham, 1986.

41. Petersen, H., *Rev. Sci. Instrum.*, **66**, 1777-1779 (1995).

42. Pieuchard, G., J. Flamand, Final report on NASA contract number NASW-2146, GSFC 283-56,777, Jobin Yvon, 1972.

43. Rah, S. Y., The authors are grateful to Dr S. Y. Rah of the Pohang Accelerator Laboratory (currently on leave at the Advanced Light Source (Berkeley)) for calculating the a_{ij}

expressions., (1997).

44. Reininger, R., V. Saile, *Nucl. Instrum. Meth.*, **A 288**, 343-348 (1990).

45. Rowland, H. A., *Phil . Mag.*, Supplement to Vol. **13** (5th series), 469-474 (1882).

46. Rowland, H. A., *Phil . Mag.*, **16** (5th series), 197-210 (1883).

47. Rudolph, D., G. Schmahl, *Umsch. Wiss. Tech.*, **67**, 225 (1967).

48. Rudolph, D., G. Schmahl, in *Progress in Optics*, Vol. **XIV**, Wolf, E., (Ed), North Holland, Amsterdam, 1977.

49. Saile, V., P. Gurtler, E. E. Koch, A. Kozevnikov, M. Skibowski, W. Steinmann, *Appl. Opt.*, **15**, 2559-2564 (1976).

50. Schultz, K., G. Kaindl, M. Domke, J. D. Bozek, P. A. Heimann, A. S. Schlachter, J. M. Rost, *Phys. Rev. Lett.*, **77**, 3086-3089 (1996).

51. SRI82, in *Proc. Int. Conf. on X-ray and VUV Synchrotron Radiation Instrumentation,* Hamburg, 1982, Nucl. Instrum. Meth. **208** (1983).

52. SRI85, *Proc. 2nd Int. Conf. on Synchrotron Radiation Instrumentation,* Stanford, 1985, Nucl. Instrum. Meth. **246** (1986).

53. SRI88, *Proc. 3rd Int. Conf. on Synchrotron Radiation Instrumentation,* Tsukuba, 1988, Rev. Sci. Instrum. 60 (1989).

54. SRI91, *Proc. 4th Int. Conf. on Synchrotron Radiation Instrumentation,* Chester, UK, 1991, Rev. Sci. Instrum. 63 (1992).

55. Welford, W., in *Progress in Optics*, Wolf, E., (Ed), Vol. **IV**, 1965.

56. Welford, W. T., *Aberrations of the symmetrical optical system*, Academic press, London, 1974.

57. West, J. B., H. A. Padmore, in *Handbook on Synchrotron Radiation*, Marr, G. V., I. H. Munro, (Eds), Vol. 2, North Holland, Amsterdam, 1987.

58. Wolfram Research Inc., 100, Trade Center Drive, Champaign, IL 61820-7237, USA.

59. Wuilleumier, F., Y. Farge, (eds.), *Int. Conf. on Synchrotron Radiation Instrumentation and New Developments*, Nucl. Instrum. Meth. 152 (1978), North Holland, Orsay, France, 1977.

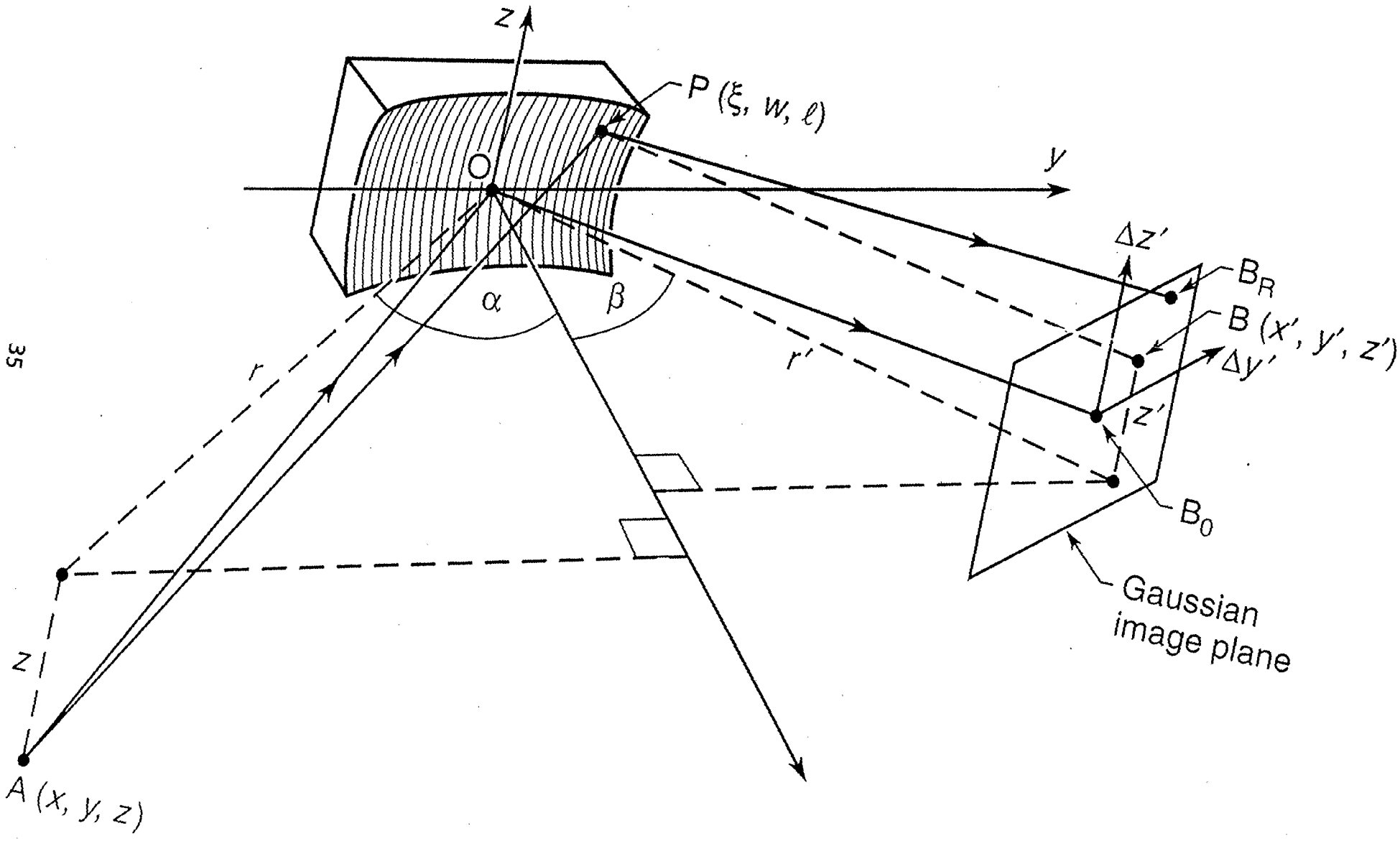
z
P (ξ, w, ℓ)
O
y
α
β
r
r′
Δz′
B_R
B (x′, y′, z′)
Δy′
z′
B_0
Gaussian
image plane
z
A (x, y, z)

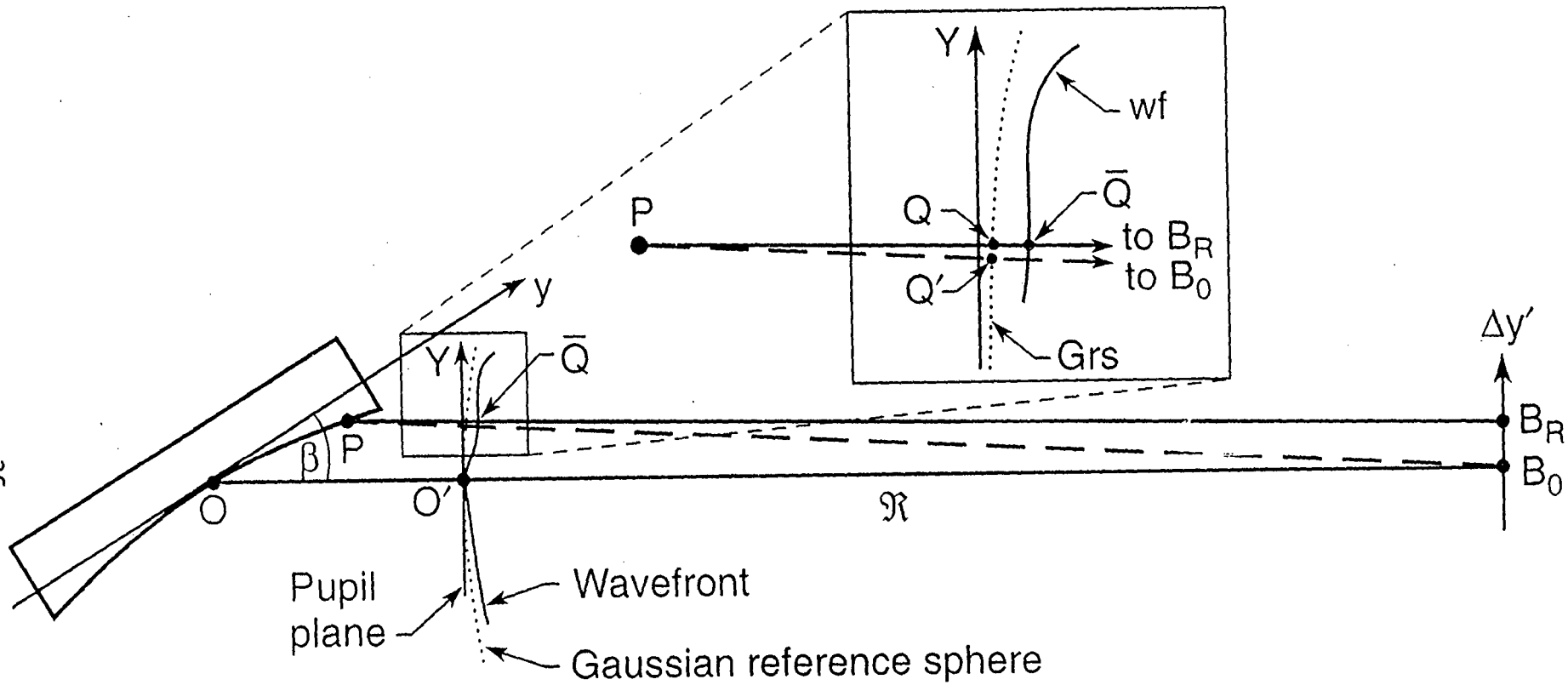

XBD 9704-01330.ILR

Figure 2

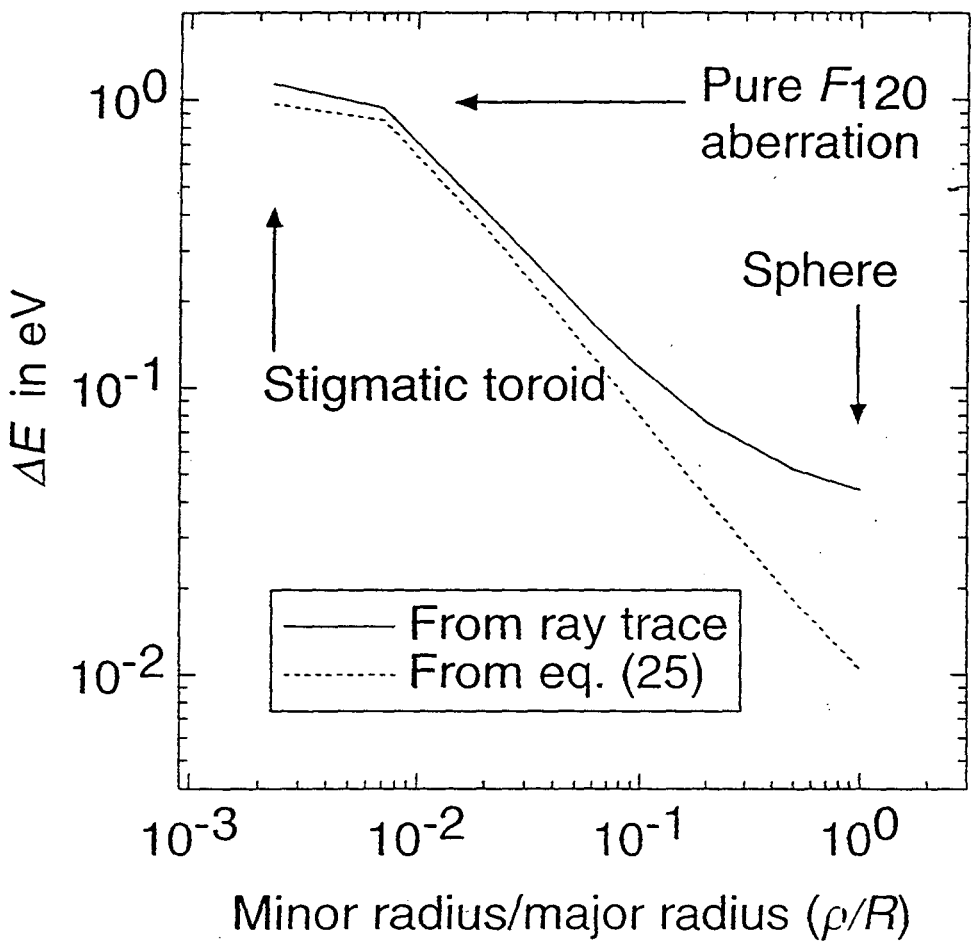
10^0
10^{-1}
10^{-2}
ΔE in eV
Pure $F120$ aberration
Sphere
Stigmatic toroid
From ray trace
From eq. (25)
10^{-3}
10^{-2}
10^{-1}
10^0
Minor radius/major radius (ρ/R)

Fi

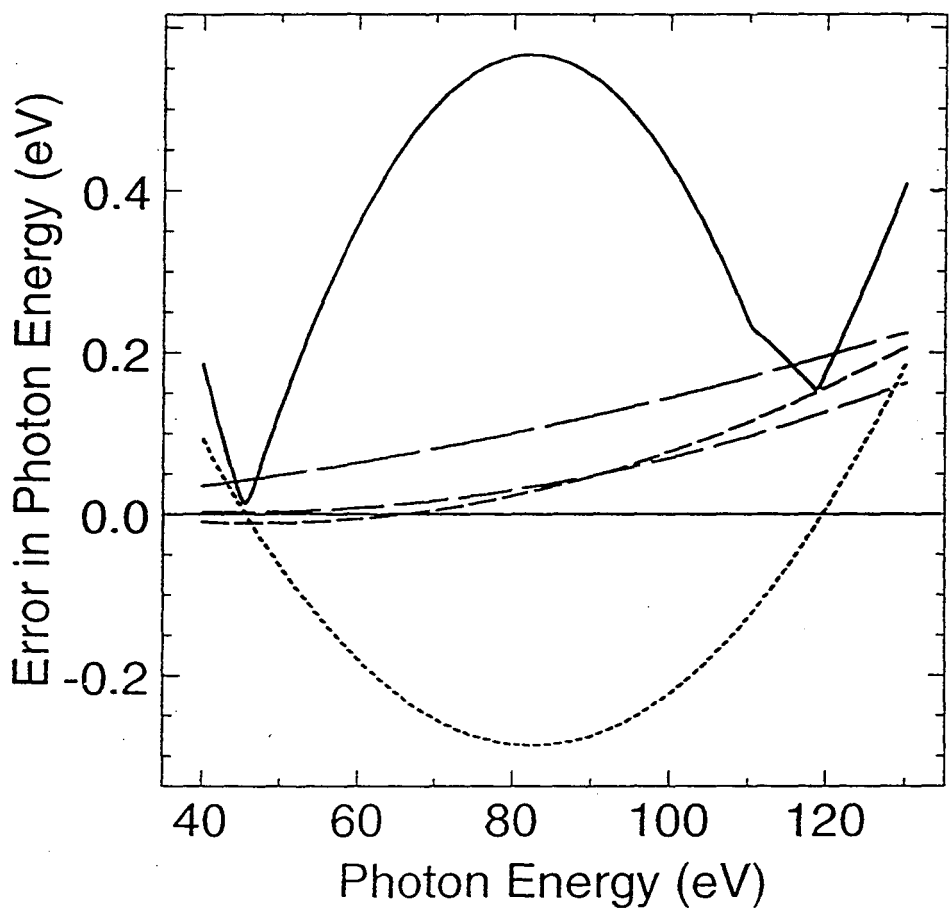
Error in Photon Energy (eV)
0.4
0.2
0.0
-0.2
40
60
80
100
120
Photon Energy (eV)

Figure 4

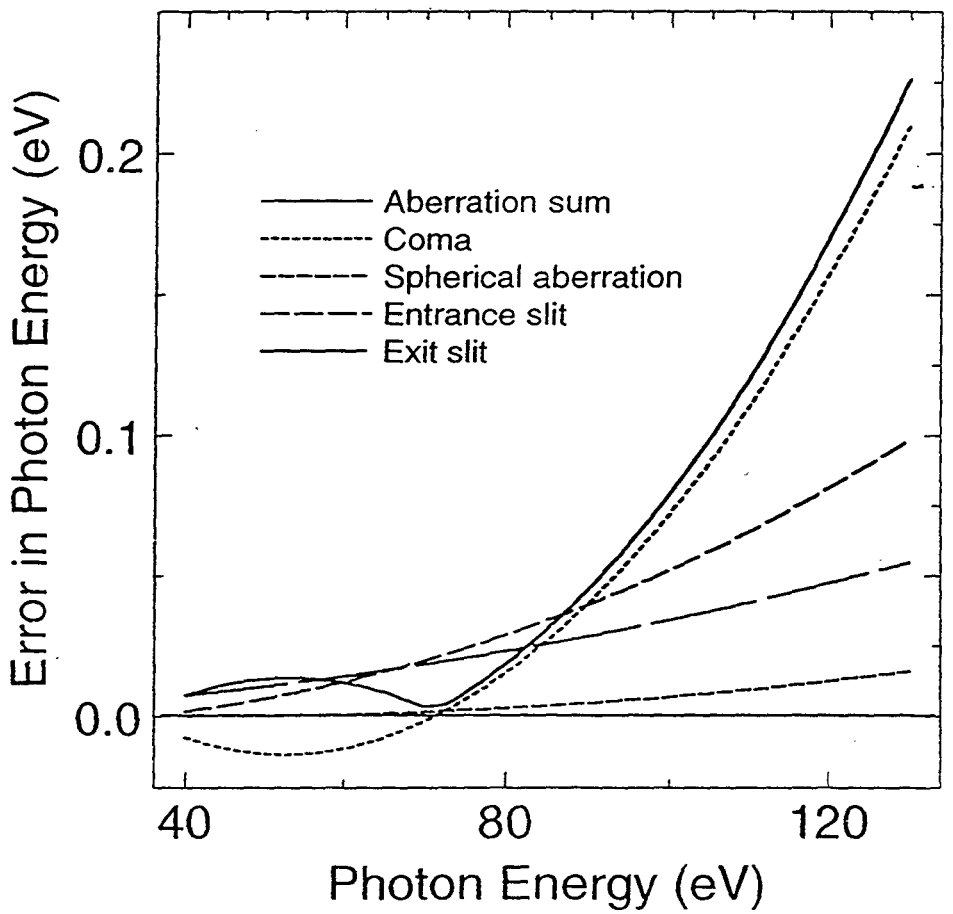
Error in Photon Energy (eV)
0.2
0.1
0.0
Aberration sum
Coma
Spherical aberration
Entrance slit
Exit slit
40
80
120
Photon Energy (eV)

Figure 5

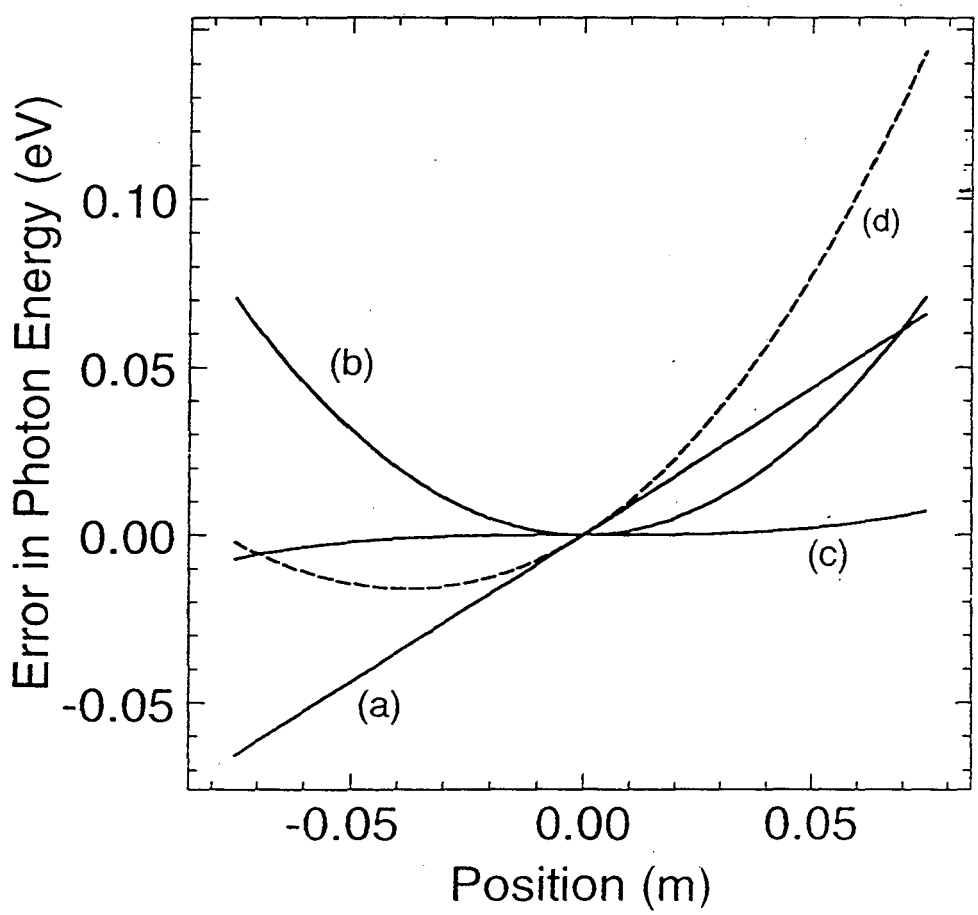
Error in Photon Energy (eV)
0.10
0.05
0.00
-0.05
(a)
(b)
(c)
(d)
-0.05
0.00
0.05
Position (m)

Figure 6

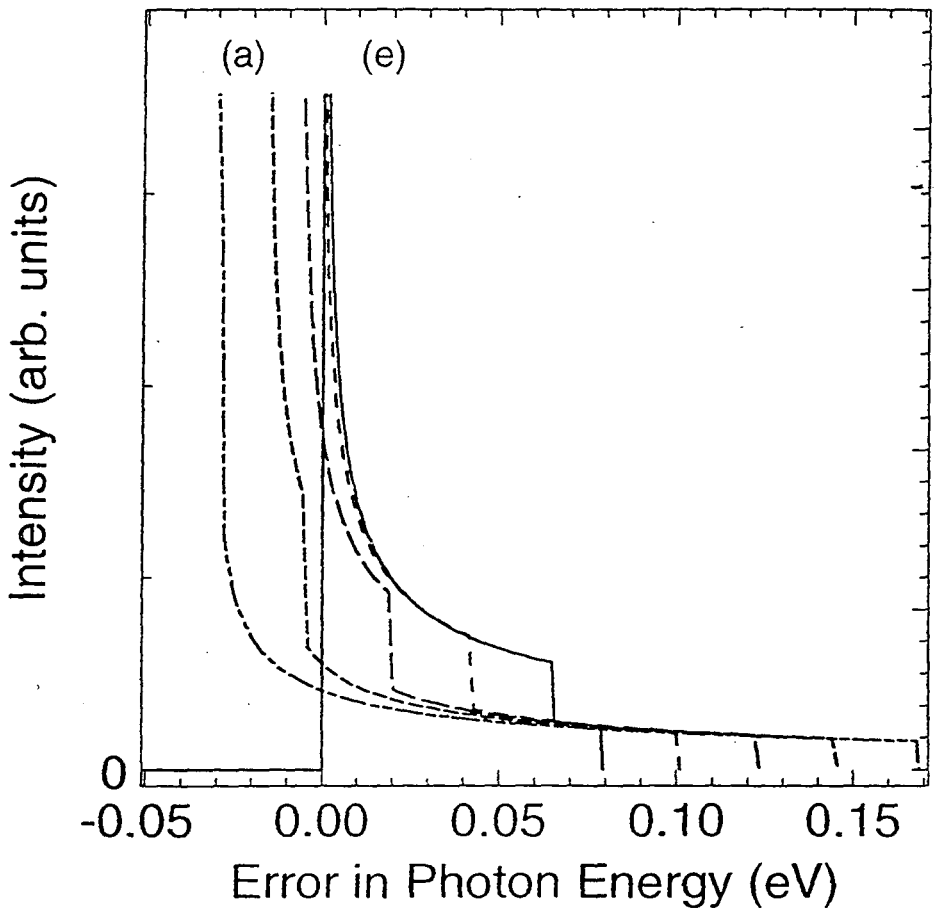
(a)
(e)
Intensity (arb. units)
0
-0.05
0.00
0.05
0.10
0.15
Error in Photon Energy (eV)

Figure 7

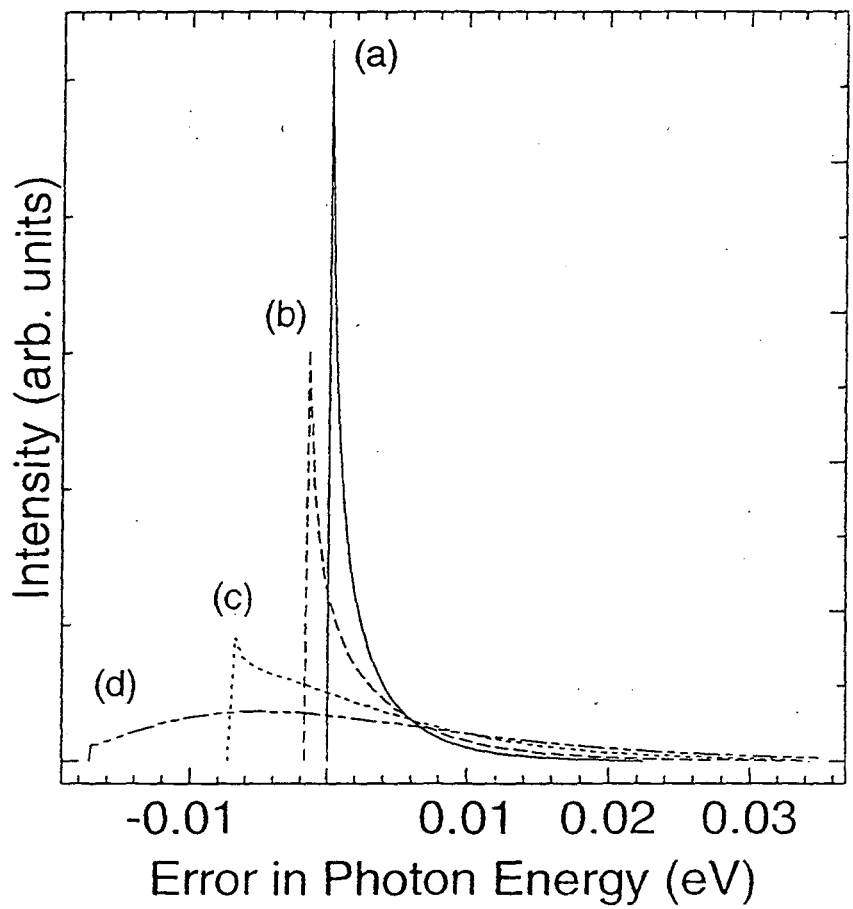
(a)
(b)
(c)
(d)
Intensity (arb. units)
-0.01
0.01
0.02
0.03
Error in Photon Energy (eV)

Figure 8

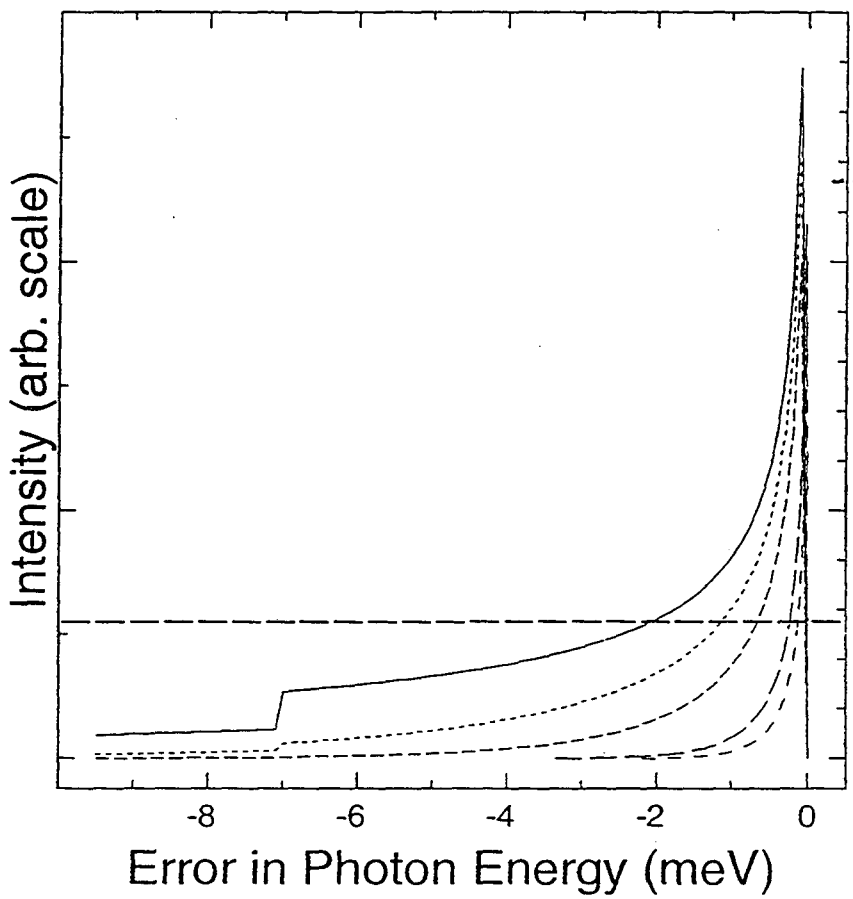

Figure 9

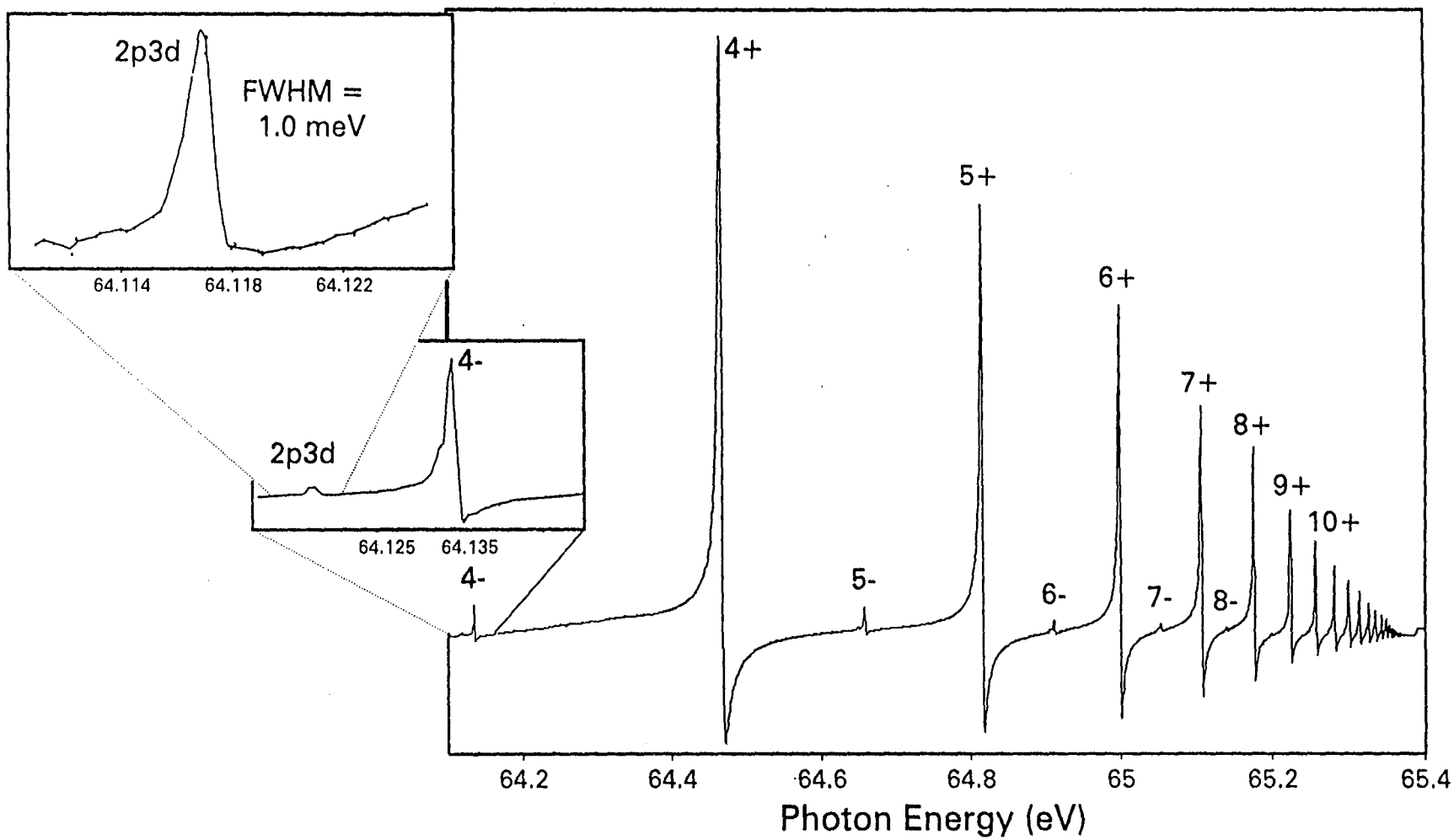
2p3d
FWHM =
1.0 meV
64.114
64.118
64.122
4-
2p3d
64.125
64.135
4+
5+
6+
7+
8+
9+
10+
4-
5-
6-
7-
8-
64.2
64.4
64.6
64.8
65
65.2
65.4
Photon Energy (eV)

Figure 10

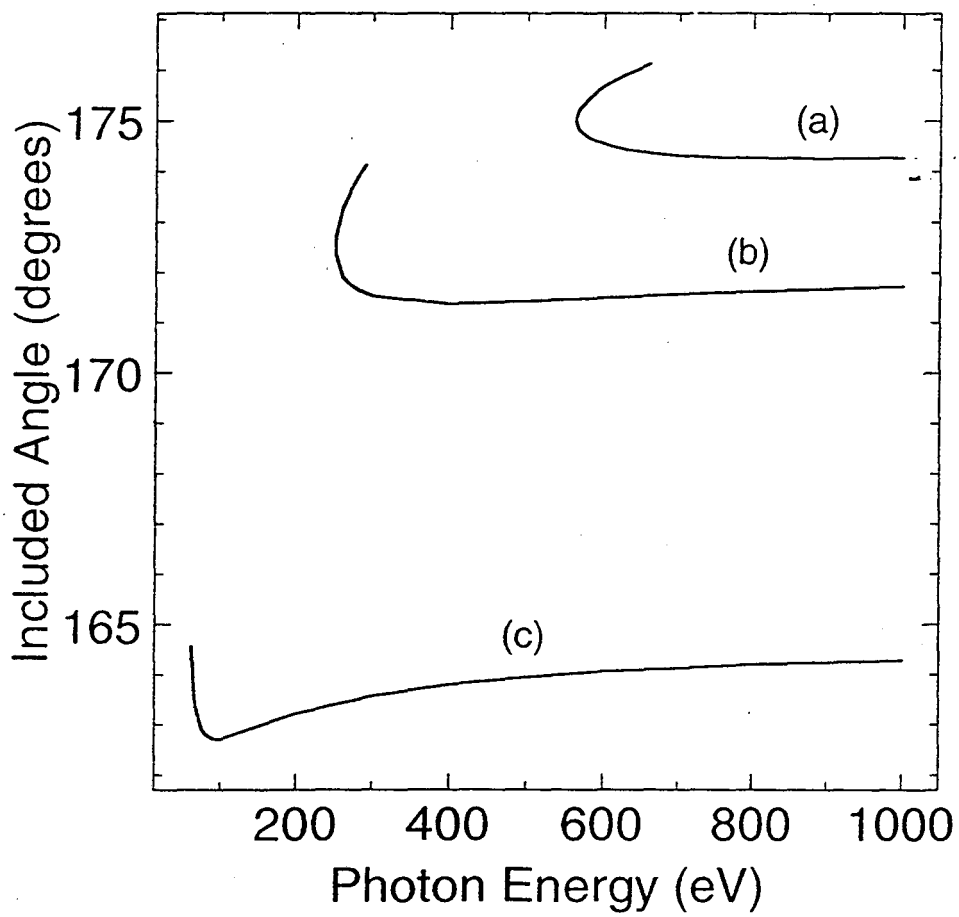
Included Angle (degrees)
175
170
165
(a)
(b)
(c)
200
400
600
800
1000
Photon Energy (eV)

Figure 11

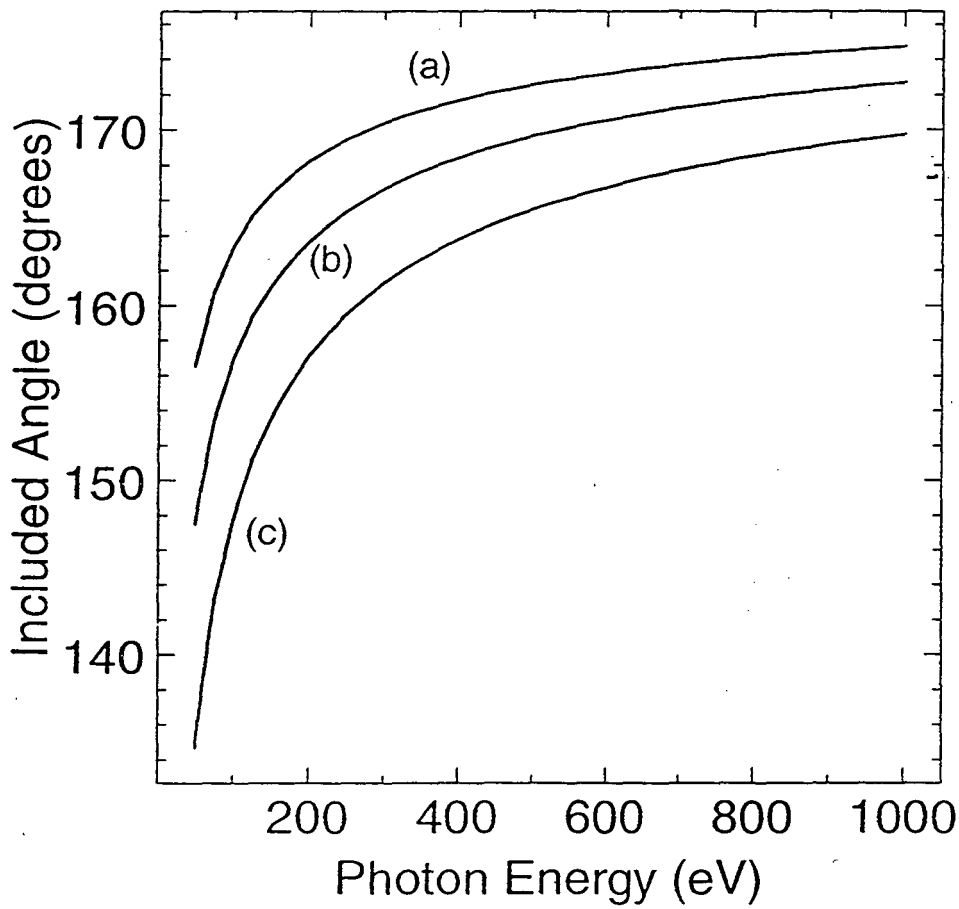
(a)
(b)
(c)
170
160
150
140
Included Angle (degrees)
200
400
600
800
1000
Photon Energy (eV)

Figure 12

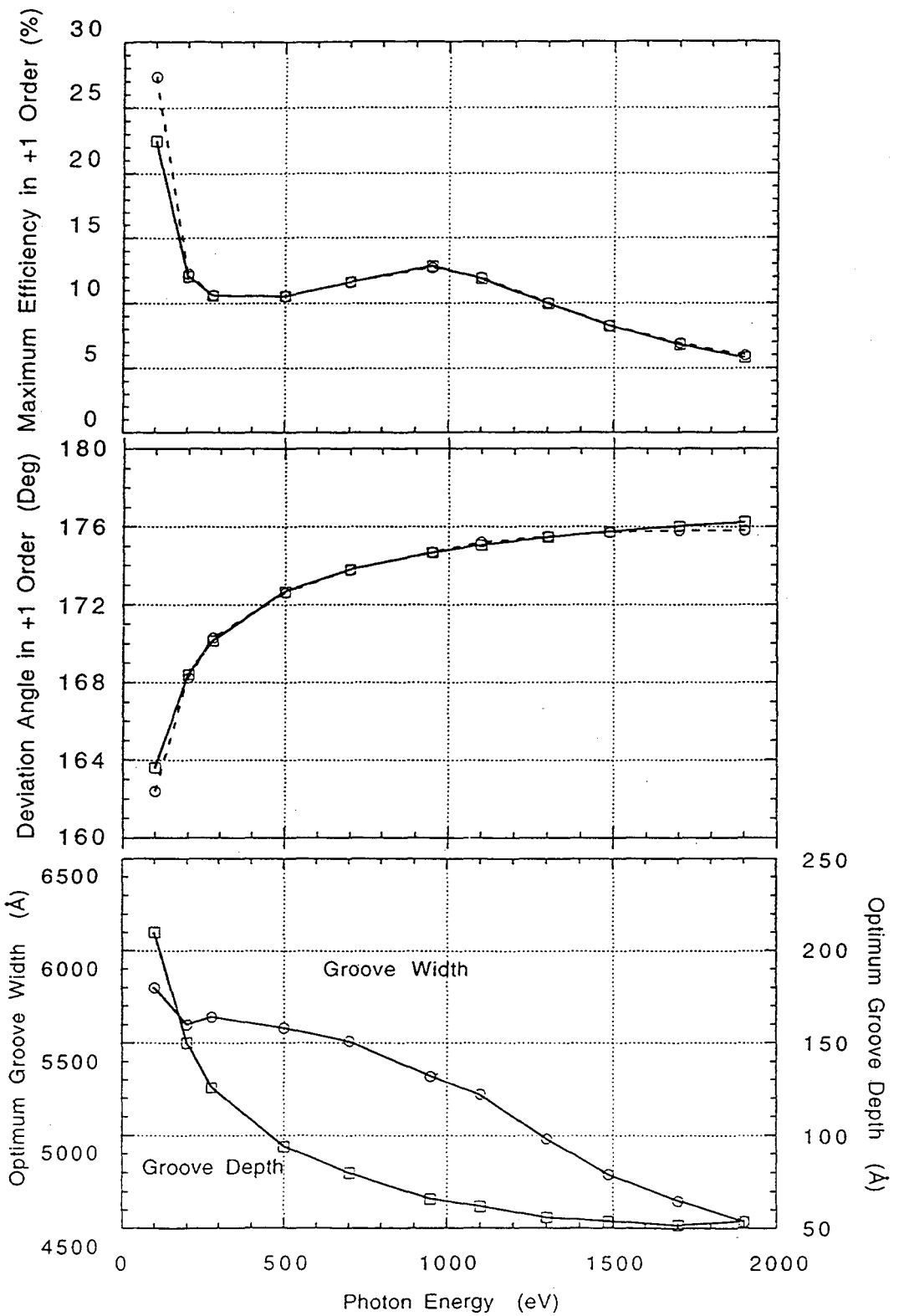
Maximum Efficiency in +1 Order (%)
30
25
20
15
10
5
0
Deviation Angle in +1 Order (Deg)
180
176
172
168
164
160
Optimum Groove Width (Å)
6500
6000
5500
5000
4500
Groove Width
Groove Depth
250
200
150
100
50
Optimum Groove Depth (Å)
0
500
1000
1500
2000
Photon Energy (eV)

Figure 13

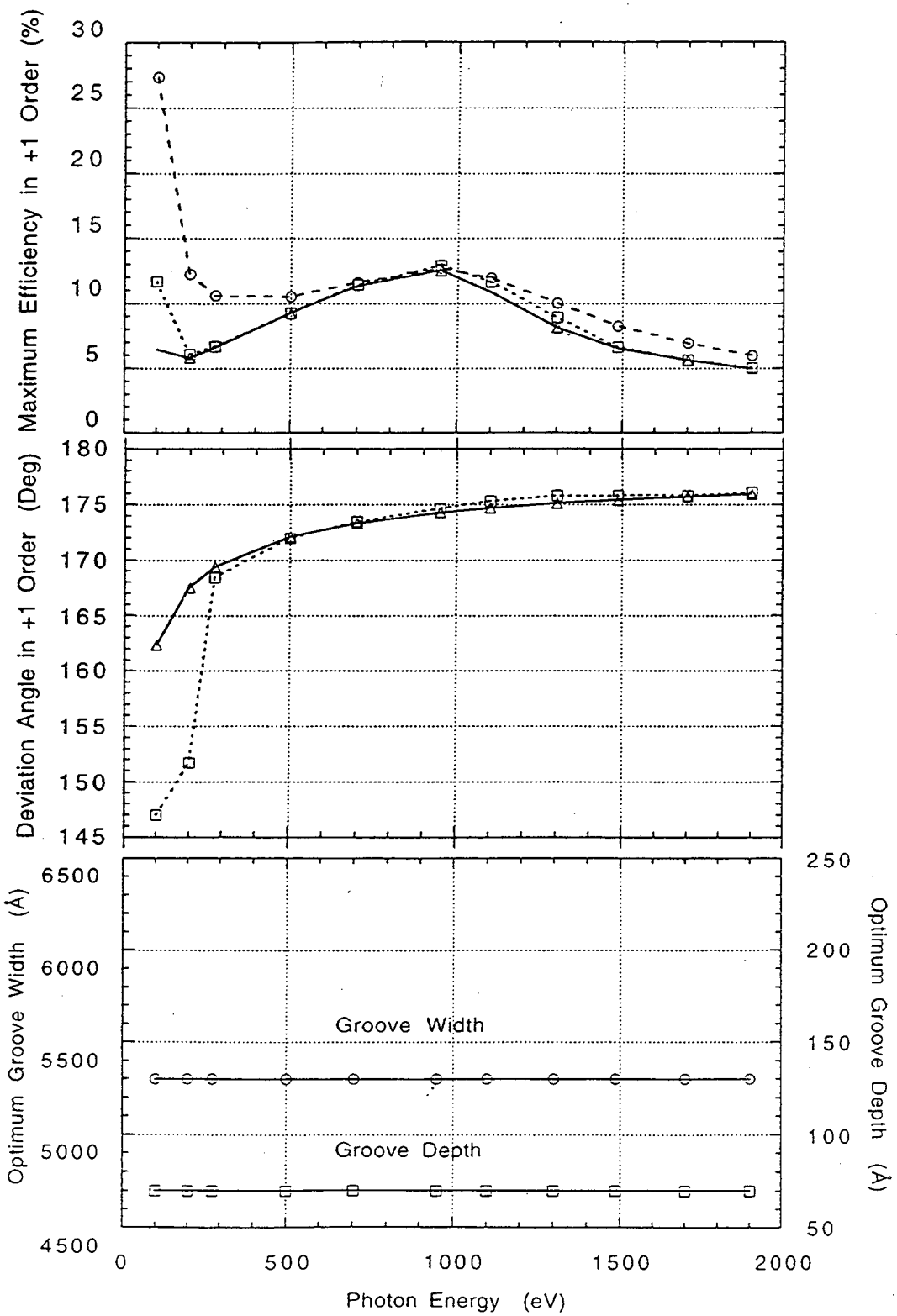
Maximum Efficiency in +1 Order (%)
30
25
20
15
10
5
0
Deviation Angle in +1 Order (Deg)
180
175
170
165
160
155
150
145
Optimum Groove Width (Å)
6500
6000
5500
5000
4500
Groove Width
Groove Depth
250
200
150
100
50
Optimum Groove Depth (Å)
0
500
1000
1500
2000
Photon Energy (eV)

Figure 14

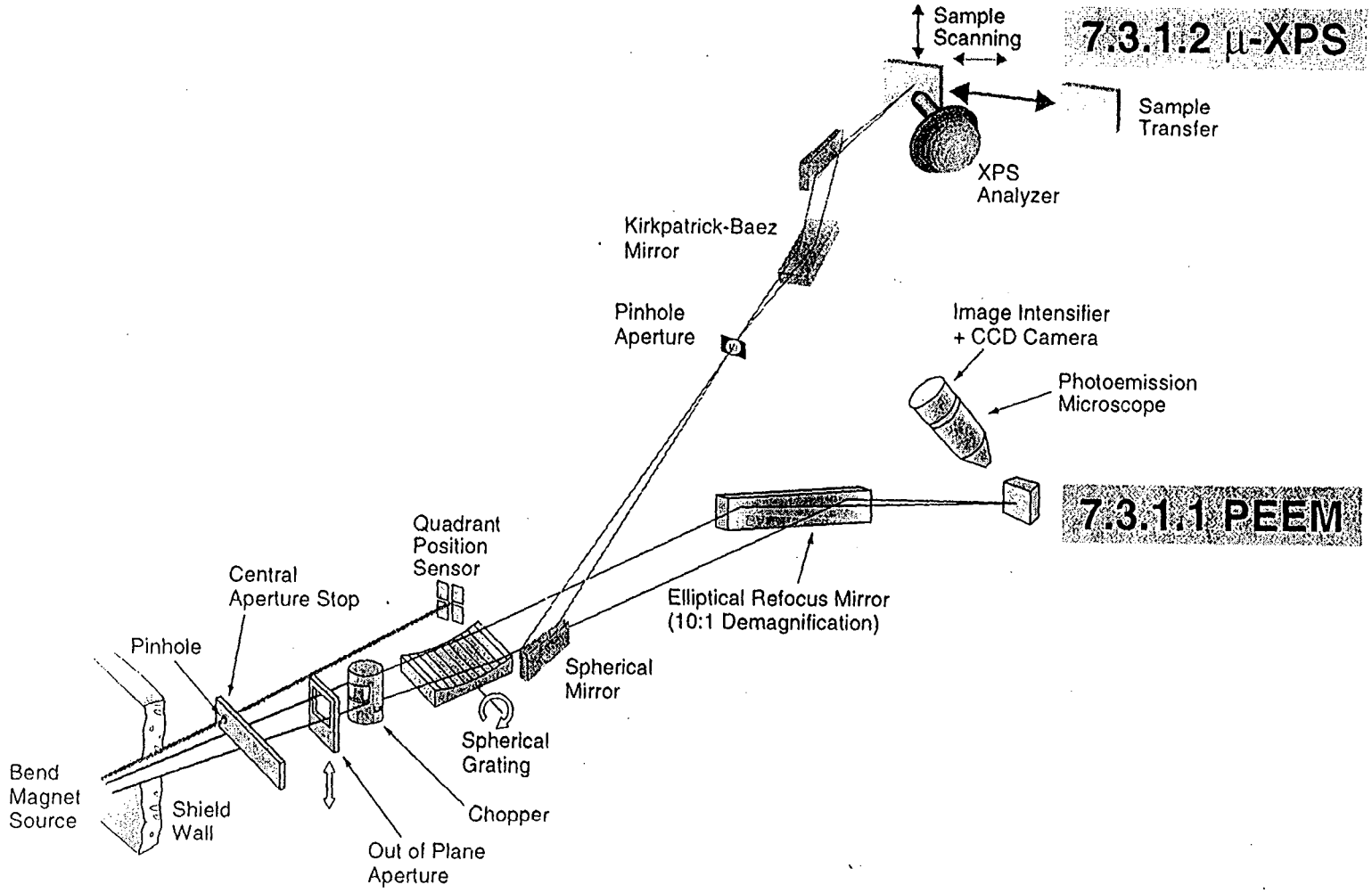
Sample
Scanning
7.3.1.2 μ-XPS
Sample
Transfer
XPS
Analyzer
Kirkpatrick-Baez
Mirror
Pinhole
Aperture
Image Intensifier
+ CCD Camera
Photoemission
Microscope
7.3.1.1 PEEM
Quadrant
Position
Sensor
Central
Aperture Stop
Elliptical Refocus Mirror
(10:1 Demagnification)
Pinhole
Spherical
Mirror
Spherical
Grating
Bend
Magnet
Source
Shield
Wall
Chopper
Out of Plane
Aperture

Figure 15

Ernest Orlando Lawrence Berkeley National Laboratory
One Cyclotron Road | Berkeley, California 94720

Prepared for the U.S. Department of Energy under Contract No. DE-AC03-76SF00098